1996ApJ...466..561M

THE ASTROPHYSICAL JOURNAL, 466:561–584, 1996 July 20
© 1996. The American Astronomical Society. All rights reserved. Printed in U.S.A.

X-RAY–IRRADIATED MOLECULAR GAS. I. PHYSICAL PROCESSES AND GENERAL RESULTS

PHILIP R. MALONEY[1]
Center for Astrophysics and Space Astronomy and JILA, University of Colorado; and National Institute of Standards and Technology, Boulder, CO 80309-0389

AND

DAVID J. HOLLENBACH[2] AND A. G. G. M. TIELENS[3]
NASA Ames Research Center, MS 245-3, Moffett Field, CA 94035
Received 1995 October 4; accepted 1996 February 1

ABSTRACT

We have modeled the physical and chemical state of dense ($n = 10^3$–10^5 cm^{-3}) neutral gas exposed to intense X-ray fluxes and the resultant infrared and submillimeter emission from the irradiated gas. The dominant parameter controlling the state of the gas in these X-ray dissociation regions (XDRs) is the ratio of local X-ray energy deposition rate to gas density; this can be expressed in terms of an effective ionization parameter. The parameter space we model ranges over 5 orders of magnitude in this ionization parameter; the gas physical conditions vary from warm, atomic, and partially ionized ($T \sim 10^4$ K, molecular hydrogen abundance $x_{H_2} \lesssim 10^{-4}$, electron abundance $x_e \sim 0.1$) to cold, molecular, and neutral ($T \sim 20$ K, $x_{H_2} \approx 0.5$, $x_e \sim 10^{-6}$). We thus cover the entire range of parameter space in which X-ray ionization and heating is important and the gas is largely neutral. Although we assume a power law for the incident X-ray flux, most of our results are independent of this assumption and are of general applicability. A wide range of diagnostic atomic and molecular line emission is produced by XDRs, which are luminous sources of infrared and submillimeter lines. This is a consequence of the large column densities ($N > 10^{22}$ cm^{-2}) that hard ($E > 1$ keV) photons are capable of penetrating before being absorbed. Strong emission lines include [Fe II] 1.26 and 1.64 μm, [O I] 63 μm, [C II] 158 μm, [Si II] 35 μm, and the 2 μm vibration-rotation lines of H_2, such as the $v = 1$–0 $S(1)$ line at 2.12 μm. We discuss diagnostic line ratios for discriminating XDRs from shocks and photodissociation regions. One strong signature of emission from XDRs is the large flux ratio ($\sim$0.1) of the major coolant line fluxes (e.g., [O I] 63 μm) to the bolometric continuum flux. XDRs are likely to be the dominant sources of emission in a range of astrophysical environments, such as molecular clouds within roughly 1 kpc of typical active galactic nuclei.

Subject headings: atomic processes — infrared: ISM: lines and bands — molecular processes — radiative transfer — X-rays: ISM

1. INTRODUCTION

Molecular gas can be exposed to X-rays in a wide range of astrophysical environments: in active galactic nuclei (AGNs), near supernova remnants or fast shocks, and in molecular clouds with embedded X-ray sources such as massive stars, young stellar objects with X-ray chromospheres, X-ray binaries, or accreting compact objects. By virtue of the large energy per photon and the large column densities ($N > 10^{22}$ cm^{-2}) that hard ($E > 1$ keV) photons are capable of traversing before absorption, X-rays can have profound effects on the chemical and thermal structure of UV-opaque molecular clouds.

The earliest investigations of the effects of X-ray irradiation on molecular gas were those of Krolik & Kallman (1983) and Lepp & McCray (1983). Krolik & Kallman investigated the effects of (relatively weak) X-ray ionization from embedded stellar sources on the chemistry and ionization balance of the Orion molecular cloud, assuming a fixed gas temperature. Lepp & McCray calculated the thermal, chemical, and ionization equilibrium of an X-ray–irradiated cloud for the specific model of a compact source of X-rays embedded in an isobaric molecular cloud. In addition, they showed that X-ray heating could be a potentially important mechanism for producing vibrationally excited molecular hydrogen emission. More recently, Krolik & Lepp (1989) examined the physical and chemical states of extremely dense molecular gas exposed to intense X-ray fluxes in the specific context of a molecular torus (see, e.g., Krolik & Begelman 1988) around the nucleus of a Seyfert galaxy. Draine & Woods (1990, 1991) performed time-dependent calculations of the evolution of an initially cold parcel of molecular gas exposed to strong X-ray emission from a supernova shock.

In this paper we re-examine the effects of X-rays on molecular gas, using significantly updated atomic and molecular data and a more thorough treatment of the physics and chemistry than earlier work. In addition, we present a much more general parameter study for a wide range of densities and X-ray fluxes, covering essentially all of the astrophysically important regime. We calculate the chemical abundances, the heating and cooling rates, the equilibrium temperature, and the intensities of important lines, and we discuss observational diagnostics for X-ray–irradiated gas. The results depend primarily on the ratio of the X-ray energy deposition rate per unit volume to the density, although the density and the column density also affect the models since they independently influence the

[1] maloney@shapley.colorado.edu.
[2] hollenbach@warped.arc.nasa.gov.
[3] tielens@dusty.arc.nasa.gov.

© American Astronomical Society • Provided by the NASA Astrophysics Data System

1996ApJ...466..561M

cooling processes. Although most of our results are of general validity, we have also calculated models using the specific assumption of a power-law X-ray spectrum in order to demonstrate the depth-dependent structure of a molecular cloud illuminated by an incident X-ray flux. The attenuation of the X-rays lowers the energy deposition rate or, equivalently, the heating and ionization rates, as a function of depth into the cloud.

Figure 1 shows schematically the structure of a dense cloud illuminated by a nearby strong X-ray source. If the cloud is exposed to a "naked" X-ray source (i.e., one with no attenuating foreground column), the surface will be highly ionized, forming an H II region. Unless the ratio of X-ray flux to gas density is low, the ionized region will not in general be followed by a FUV-produced photodissociation region (PDR), as the X-rays will dominate over the FUV photons. In the remainder of the cloud ($N_H \approx 1$–2×10^{22} cm^{-2} for a typical giant molecular cloud), X-rays will dominate the heating of the gas and the chemical composition, through X-ray dissociation and ionization. We will call such regions X-ray dissociation regions or XDRs. If this cloud is shielded from the direct light of the X-ray source by, e.g., a circumnuclear torus or a shadowing cloud, the H II region and the PDR (if any) will not be present. The physical conditions in the XDR will depend on the X-ray flux and the density of the gas, ranging from warm ($T \approx 10^4$ K), largely atomic ($x_{H_2} \lesssim 10^{-4}$), partially ionized ($x_e \sim 0.1$) gas for high ratios of flux/density to cool (10 K), molecular ($x_{H_2} \approx 0.5$), largely neutral ($x_e \lesssim 10^{-6}$) gas for low ratios.

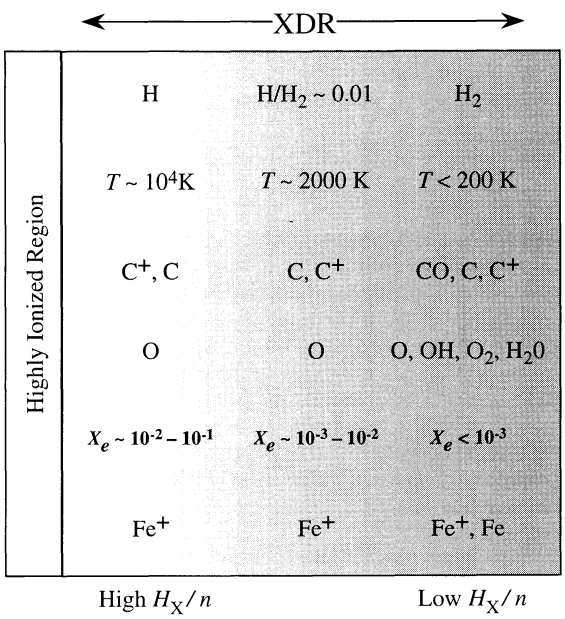

FIG. 1.—Schematic structure of an X-ray dissociation region (XDR). The approximate temperature, chemical composition, and ionization fraction are shown as a function of the ratio of the local X-ray energy deposition rate per particle H_X to the total hydrogen density n (see § 2.1.1). The X-ray flux-to-density ratio decreases from left to right. At very high values of H_X/n (which we do not consider), there will be a highly ionized surface region in which any ionizing UV continuum is also absorbed. If a high column density cloud is exposed to a sufficiently intense X-ray continuum, this schematic XDR will approximate the actual structure of the cloud, with H_x/n decreasing because of absorption with increasing column density into the cloud. Such a gradient in H_X/n will also result from, e.g., increasing distance from an X-ray source, as in the case of molecular clouds in the disk of a galaxy containing an active nucleus.

Our results have very general applicability. For example, Seyfert galaxies, in which X-ray irradiation of dense neutral clouds is likely to be a very important process, have typical X-ray luminosities $L_X \sim 10^{44}$ ergs s^{-1} (Mushotzky, Done, & Pounds 1993). Hence, the X-ray flux incident on molecular clouds near the nucleus is $F_X \approx 84 L_{44} r_2^{-2}$ ergs cm^{-2} s^{-1}, where the X-ray luminosity is $10^{44} L_{44}$ ergs s^{-1} and the distance to the X-ray source is $10^2 r_2$ pc. We will study a range from $F_X \sim 0.1$–10^6 ergs cm^{-2} s^{-1} in our models. The interstellar medium pressure in AGNs is much higher than in the solar neighborhood, and consequently molecular cloud densities will generally be higher as well ($n \sim 10^4$–10^5 cm^{-3}, compared to $n \sim 10^3$ cm^{-3} for molecular clouds in the solar neighborhood). In our models, we will consider densities in the range 10^3–10^5 cm^{-3}. Our results are equally relevant for gas on a size scale of 20 AU surrounding a T Tauri star with a typical X-ray luminosity of 10^{32} ergs s^{-1} (i.e., solar nebula–like regions), for gas on a size scale of $r \sim 0.1$–1 pc around the "Great Annihilator" source in the Galactic center ($L_X \approx 5 \times 10^{37}$ ergs s^{-1}), and for molecular cloud regions ($r \approx 1$ pc) exposed to the X-ray flux from strong supernova shocks ($L_X \sim 10^{36}$–10^{40} ergs s^{-1}).

In § 2 we discuss the important physical processes operating in the gas, including the X-ray ionization and heating rates, the important cooling mechanisms, and the grain and gas-phase chemistry. We specify the choice of model parameters in § 3, while our results (both analytical and numerical) are presented in § 4. We also discuss the differences between emission from XDRs and from shocks and PDRs. We summarize our results and conclusions in § 5.

2. PHYSICAL PROCESSES

A large number of physical and chemical processes are important in dense gas illuminated by X-rays. In this section we outline the important gas and grain physics and sketch out the X-ray photon-gas interactions (the energy deposition and loss routes). In addition, we estimate the magnitude of the X-ray ionization and heating rates for a typical region in which irradiation by X-rays dominates the chemical and thermal balance of the interstellar medium.

2.1. *X-Ray Processes*

2.1.1. *Energy Deposition, Ionization, and Heating Rates*

The physical and chemical state of a parcel of dense gas illuminated by X-rays is generally insensitive to the actual shape of the X-ray spectrum, depending mostly on the ratio of the local X-ray energy deposition rate per particle, H_X, to the gas density n. This approximate behavior follows from simple physics for the chemical and thermal balance: the molecular destruction and heating rates per unit volume due to X-ray–induced ionization are proportional to nH_X, whereas the molecular formation and cooling rates are generally proportional to n^2 times a rate coefficient. Hence, the most important parameter in calculating the equilibrium temperature or chemical abundances is H_X/n, although the results do not scale exactly with this parameter because of the effects of collisional suppression of coolants, radiative trapping, and complicated (e.g., chemical) destruction mechanisms. As our concern in this paper is the effects of the X-rays on molecular gas, we will always assume that there is an attenuating column of at least $N_{att} \sim 10^{21}$ cm^{-2}

© American Astronomical Society • Provided by the NASA Astrophysics Data System

1996ApJ...466..561M

between the photon source and the parcel of gas being modeled. Thus, any normal UV photon–dominated region (the H II region and/or a photodissociation region) will lie interior (in column density) to our modeled regions.

The magnitude of H_X—and hence the ionization and heating rates—can be estimated for an interesting example as follows. Consider the case of molecular clouds within a few hundred parsecs of an active nucleus, assumed to have a power-law X-ray spectrum. For X-ray photon energies $E \lesssim 10$ keV (i.e., attenuating column densities $N_{att} \lesssim 10^{24}$ cm^{-2}), the dominant interaction of the X-ray photons with matter is through photoelectric absorption; at higher energies, Compton scattering dominates. We have adopted the X-ray photoelectric cross section per hydrogen nucleus σ_{pa} of Morrison & McCammon (1983), which is essentially that of cold neutral matter; this is a good approximation for the range of parameter space with which we are concerned. For convenience we have fitted a broken power law to the cross section as a function of energy (Appendix A). For a chosen set of elemental abundances, the X-ray opacity is essentially independent of the degree of depletion into grains (Morrison & McCammon 1983). Assuming that Auger electrons contribute an energy equal to the photoionization threshold, H_X is just given by

$$H_X = \int_{E_{min}}^{E_{max}} \sigma_{pa}(E)F(E)dE \ , \tag{1}$$

where $F(E)$ is the local photon energy flux per unit energy interval. For typical giant molecular cloud column densities of $N_H \approx 10^{22}$ cm^{-2}, nearly all photons with energies $E \lesssim 1$ keV will be absorbed before the cloud center is reached. For a power law, the photoionization is always dominated by the lowest energy photons that have not yet been attenuated, so assume that all of the ionization is due to photons with $E \geq E_1$, where E_1 is the energy at which the photoelectric absorption optical depth $\tau(E) = 1$, and ignore attenuation for photon energies above E_1. Assuming equal energy per decade in hard X-rays (as is approximately true for AGNs) and a total 1–100 keV X-ray luminosity of $L_X = 10^{44}L_{44}$ ergs s^{-1}, the energy deposition rate per particle at cloud center (using the cross section [A5c]) is approximately

$$H_X \sim 7 \times 10^{-22} L_{44} r_2^{-2} N_{22}^{-1} \text{ ergs s}^{-1} \ , \tag{2}$$

where $N_{att} = 10^{22}N_{22}$ cm^{-2} is the column density of hydrogen attenuating the X-ray flux. Note the slow (N_{att}^{-1}) decline of the energy deposition rate with column density compared to the exponential attenuation of FUV photons by dust grains in a PDR.

The total ionization rate per particle, ζ_T, is proportional to H_X. The *primary* ionization rate is just given by the integral over energy of the local X-ray photon flux per unit energy $F(E)/E$ times the photoabsorption cross section. A unique feature of X-ray irradiation of neutral gas is that the ionization rate of hydrogen is dominated by the *secondary* ionizations generated by the primary photoelectrons. This is a consequence of the large primary photoelectron energies, which are typically $\sim$keV. If the ionization fraction of the gas $x_e \lesssim 1\%$, approximately 40% of the primary photoelectron energy goes into ionization, whether the gas is atomic (Shull & van Steenberg 1985, hereafter SvS85) or molecular (Voit 1991a, hereafter V91). Thus, the number of secondary ionizations $N_{sec} \approx 26(30)$ per keV of primary photoelectron energy for molecular (atomic) hydrogen, and secondary ionizations always dominate by a large factor over primary ionizations in gas with a low ionization fraction. Ignoring the primary ionization rate compared to the secondaries, the total hydrogen ionization rate simplifies to

$$\zeta_T \simeq N_{sec}(x_e)H_X \ , \tag{3}$$

where N_{sec}, the number of secondary ionizations per unit of primary photoelectron energy, has been taken to be independent of energy. The secondary ionization rate is a function of the ionization fraction; above $x_e \sim 1\%$, an increasing fraction of the primary photoelectron energy is lost to Coulomb interactions with the ambient thermal electrons and goes into gas heating. In the low-ionization limit, the X-ray ionization rate in our example problem is

$$\zeta_T \sim 1.4 \times 10^{-11} L_{44} r_2^{-2} N_{22}^{-1} \text{ s}^{-1} \ . \tag{4}$$

For reference, with the default values of all parameters, this is $\sim 10^6$ times larger than the cosmic-ray ionization rate in solar neighborhood molecular clouds (Black 1987).

Only a fraction of the energy locally deposited by the X-rays will go into heating the gas. The remainder will lead to excitation and will be lost through radiation that is ultimately mostly absorbed by dust. Like ionization, the heating and excitation rates due to the nonthermal primary and secondary electrons are functions of both the ionization fraction of the gas and its composition (atomic or molecular). Figure 2 shows a flow chart indicating the energy deposition and loss routes for the atomic and molecular cases. When the gas is largely ionized (x_e close to unity), nearly all of the primary photoelectron energy is deposited as heat, through Coulomb interactions with the ambient thermal electrons. As the ionization fraction decreases, heating via Coulomb losses drops, and losses to ionization and electronic and line excitation become important: in the low-ionization limit, about 40% goes into ionization and a somewhat larger fraction (close to 50%) goes into excitation (electronic excitations of H and electronic, vibrational, and rotational excitations of H_2), with the remainder going into ionization and excitation of He and heat.

In a pure atomic hydrogen gas, once the nonthermal electron energy drops below the threshold for excitation of Lyα (10.2 eV), all of the remaining secondary electron energy goes into heating. This is the only heating process for neutral atomic gas, so the X-ray heating efficiency is relatively low in atomic gas when the ionization fraction is small: in the limit $x_e = 0$, about 10% of the primary photoelectron energy goes into Coulomb heating (i.e., about 5 eV per secondary ionization; Xu & McCray 1991, hereafter XM91).

However, in a completely molecular gas, the heating efficiency is much larger. The primary reason for this is that much of the ionization energy may go into heating in a molecular gas. When a proton radiatively recombines, the recombination energy emerges as a photon and is lost to the gas. However, in a molecular gas, the H_2^+ ion created by a secondary ionization will react with a hydrogen molecule to produce H_3^+,

$$H_2^+ + H_2 \rightarrow H_3^+ + H \ . \tag{5a}$$

The H_3^+ ion may either dissociatively recombine with an electron or react with one of the abundant species in the gas to produce another molecular ion, but in either case the end result is the same: the molecular ion dissociatively recom-

© American Astronomical Society • Provided by the NASA Astrophysics Data System

1996ApJ...466..561M

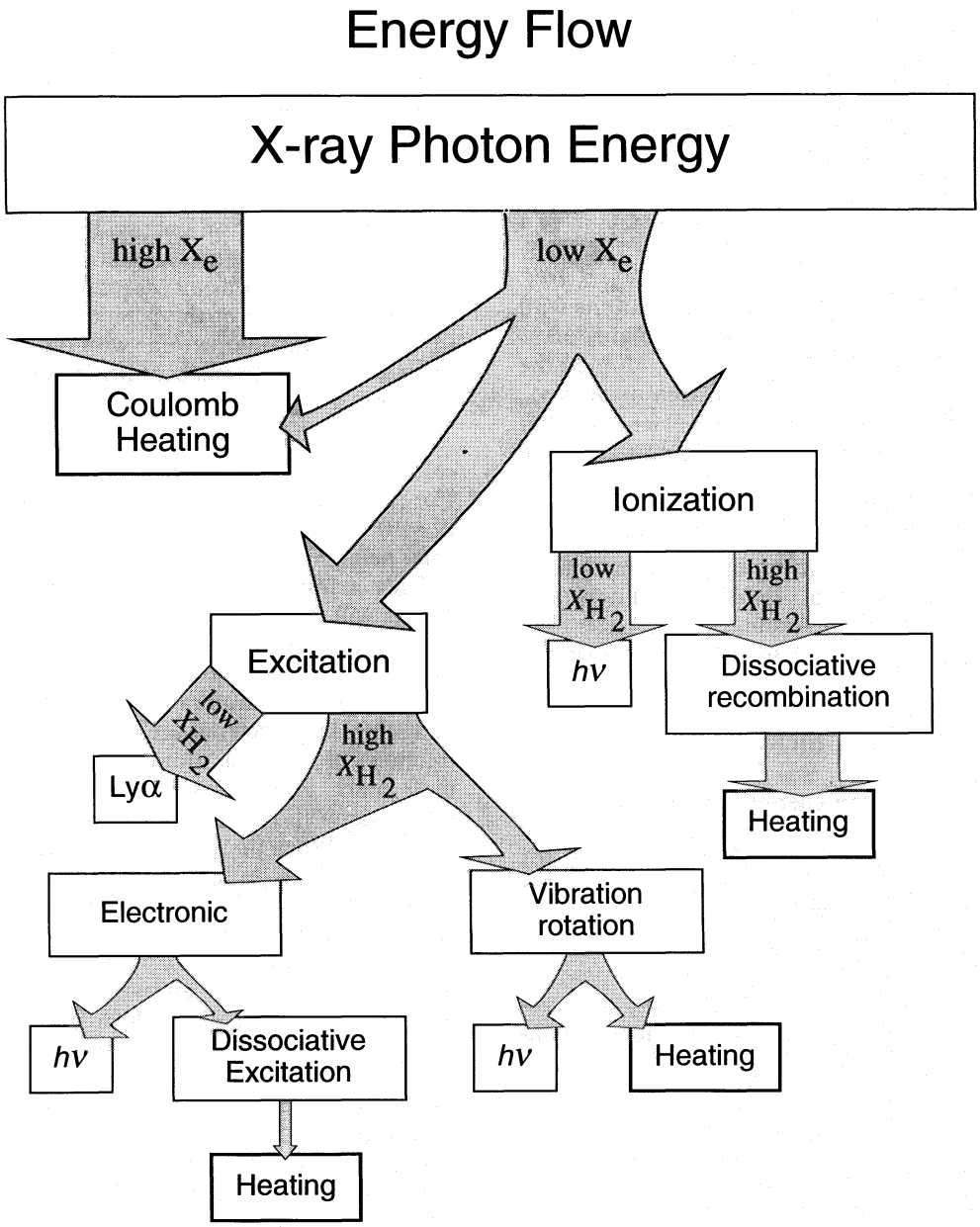

FIG. 2.—Flow chart illustrating the loss routes for energetic electrons in dense atomic and molecular gas. The widths of the arrows indicate the approximate fractions of the primary photoelectron energy that are deposited in the indicated processes, with branching depending on the value of the electron fraction x_e and the molecular hydrogen fraction x_{H_2}. The energy that goes into exciting the vibration-rotation lines of H_2 is thermalized if the gas density is above the relevant critical densities; otherwise, it emerges in emission lines (see § 2.1.1).

bines with an electron, so that much of the ionization energy goes into the kinetic energy of the reaction products (Glassgold & Langer 1973). The exothermic yield of equation (5a), followed by dissociative recombination, is 11 eV. Following Glassgold & Langer, we assume that 2 eV goes into vibrational excitation of both the H_3^+ and H_2 that are formed. Since dissociative recombination of H_3^+ goes to $H_2 + H$ and $H + H + H$ with equal probability, with these assumptions, 8 eV per ionization goes into gas heating.

In addition, significant amounts (up to $\approx 10\%$) of the primary nonthermal photoelectron energy can go into excitation of the rotation-vibration bands of H_2; if the gas density is above the critical densities for these transitions, then much of this energy will also be thermalized. (This is also true of the energy going into vibrational excitation of H_2 because of the dissociative recombination reactions discussed above.) Energy is also deposited into the gas by excitations to dissociative electronic states (e.g., the triplet states). The relevant product energies have been taken from Cravens, Victor, & Dalgarno (1975) and Stephens & Dalgarno (1973); this can amount to a few percent of the primary photoelectron energy. Recall that at low x_e, about 40% of the primary photoelectron energy goes into ionization, so in fully molecular gas the heating efficiency f_h is $\sim 30\%$–40%, depending slightly on density because of collisional deexcitation.

In a partly atomic, partly molecular gas, an H_2^+ ion may charge exchange with a hydrogen atom,

$$H_2^+ + H \rightarrow H_2 + H^+ . \quad (5b)$$

Equations (5a) and (5b) are equally important when about 15% of the hydrogen is molecular. The proton ionization

© American Astronomical Society • Provided by the NASA Astrophysics Data System

1996ApJ...466..561M

energy is lost to the gas. The fractional loss rates to ionization, excitation, and Coulomb heating are taken from SvS85 and XM91 for atomic gas and V91 for molecular gas, weighted by the appropriate fractional abundances for a partially molecular gas.

The X-ray photoionization heating rate per particle is of the same form as equation (3), with $N_{\rm sec}$ replaced by f_h, the fraction of primary photoelectron energy going into gas heating. The heating rate per particle in our example problem is

$$\Gamma_{\rm X} \sim 2 \times 10^{-22} L_{44} r_2^{-2} N_{22}^{-1} \text{ ergs s}^{-1} , \quad (6)$$

where we have taken $f_h \sim 0.3$. Like the ionization rate, the heating rate is roughly 6 orders of magnitude larger than the solar neighborhood cosmic-ray heating rate (Black 1987). The heating per *total* ionization is similar for X-ray ionization and cosmic-ray ionization (Cravens & Dalgarno 1978).

2.1.2. *UV Photon Flux from Secondary Electrons*

The chemistry in X-ray–illuminated neutral clouds is significantly affected by the *internally* generated FUV (6 eV $\lesssim h\nu \lesssim$ 13.6 eV) photons produced by energetic nonthermal electrons colliding with hydrogen atoms and molecules (Prasad & Tarafdar 1983). These collisions result in the emission of Lyα and Lyman-Werner band photons, which photodissociate and photoionize molecules and trace atoms.

For gas with an electron fraction $x_e \lesssim 0.01$, about 40% of the energy deposited by X-rays results in the production of these FUV photons. The net result is that the dense, opaque (to FUV) interiors of X-ray–illuminated clouds can chemically resemble photodissociation regions (PDRs; see Tielens & Hollenbach 1985) with iron, silicon and carbon in the singly ionized state and large abundances of neutral atomic oxygen. Like PDRs, most of the FUV is absorbed by dust (assuming standard local ISM dust properties) and emerges as IR continuum. However, the gas in PDRs is generally heated by the FUV-induced grain photoelectric heating mechanism, whereas the X-ray–illuminated gas is heated by the X-ray–induced photoelectrons from the gas. The result is that X-ray–illuminated clouds receive a much higher ratio ($\sim$0.1–1) of gas heating to grain heating compared with PDRs, where the ratio is $\sim 10^{-3}$ to 10^{-2} (Tielens & Hollenbach 1985). Therefore, the ratio of the strong cooling lines to the IR continuum will be much larger in X-ray–illuminated gas than in PDRs. Another difference is that the FUV produced in atomic gas is nearly entirely Lyα, which is not sufficiently energetic to ionize carbon or sulfur. Therefore, the atomic carbon and sulfur abundances tend to be larger in the atomic zones of XDRs than in PDRs.

The important parameter in the chemistry and physics of PDRs is G_0/n, the ratio of the (normalized) FUV photon flux to the gas density (Tielens & Hollenbach 1985). For the internal FUV field generated by the X-rays, this ratio is simply related to $H_{\rm X}/n$:

$$G_0/n = 6 \times 10^{23} f_{\rm UV} H_{\rm X}/n \text{ cm}^3$$
$$\approx 5 \times 10^{-5} f_{\rm UV} F_{\rm X} N_{22}^{-1} n_5^{-1} \text{ cm}^3 , \quad (7)$$

where $f_{\rm UV}$ is the fraction of the deposited X-ray energy that is converted to FUV photons, $H_{\rm X}/n$ is in cgs units, $10^5 n_5$ cm^{-3} is the total density of hydrogen nuclei, and G_0 is the FUV energy flux normalized to 1.6×10^{-3} ergs cm^{-2} s^{-1} so that $G_0 \sim 1$ represents the local ambient interstellar FUV flux. For H II regions, reflection nebulae, and PDRs in starburst galactic nuclei, G_0/n is of order unity, considerably larger than the typical value in XDRs.

We have adopted the treatment of Gredel et al. (1989) for the effects of the internally generated FUV. For all species except CO, the photoreaction rate per atom or molecule for a given species m is given by

$$R_m = (2.6\psi_{\rm LyW} p_m x_{\rm H_2} + \psi_{\rm Ly\alpha} p_a x_{\rm H})\zeta_T (1-\omega)^{-1} \text{ s}^{-1} , \quad (8)$$

where $\psi_{\rm LyW}$ and $\psi_{\rm Ly\alpha}$ are the ratios of the number of Lyman-Werner or Lyα photons produced per H_2 or H ionization, ζ_T is the total ionization rate assuming secondaries dominate, $x_{\rm H_2}$ is the H_2 abundance relative to H nuclei, $x_{\rm H}$ is the H abundance, p_m is the ratio of the cross section of species m for reaction with Lyman-Werner photons to the grain cross section per H nucleus, p_a is the Lyα equivalent to p_m, and ω ($\sim$0.5) is the grain albedo. Table 1 lists the reactions included and the values of p_m and p_a adopted. The values of $\psi_{\rm LyW}$ and $\psi_{\rm Ly\alpha}$ vary slightly with ionization fraction, but typically $\psi_{\rm LyW} \simeq 1.4$ and $\psi_{\rm Ly\alpha} \simeq 1.2$.

For CO we have crudely fitted the self-shielding results of Gredel, Lepp, & Dalgarno (1987) to obtain

$$R_{\rm CO} = 2.7 x_{\rm CO}^{-1/2} T_3^{1/2} x_{\rm H_2} \zeta_T \text{ s}^{-1} , \quad (9)$$

where $x_{\rm CO}$ is the CO abundance and $T = 1000 T_3$ K is the gas temperature.

2.1.3. *Excitation of Molecular Hydrogen Vibration-Rotation Levels*

The nonthermal electrons generated by X-ray photoionization can excite emission in the vibration-rotation bands of molecular hydrogen via collisions. This may occur either by direct collisional excitation from the ground rotation and vibration states or by cascade following collisional excitation of excited electronic states. In the first case, the apparent excitation temperature is determined by the relative collisional excitation cross sections; for example, the ratio of the $v = 2$ and $v = 1$ levels will always correspond to $T_{\rm ex} \approx 1700$ K when direct nonthermal excitation dominates, independent of the gas kinetic temperature (V91). In the case of a cascade from an excited electronic state, the excitation is fixed largely by the values of the Einstein A-coefficients (ignoring multiple pumps) so that the level distribution is essentially the same as in the case of UV pumping of the electronic states (Black, Porter, & Dalgarno

TABLE 1

INTERNALLY GENERATED FUV REACTIONS

Reaction	p_a[a]	p_m[b]
OH + FUV → O + H	1000	509
H_2O + FUV → OH + H.....	3700	971
O_2 + FUV → O + O	750	751
CH + FUV → C + H.....	350	730
C + FUV → $C^+ + e^-$	0	510
Fe + FUV → $Fe^+ + e^-$	300	447
Ni + FUV → $Ni^+ + e^-$	300	447
S + FUV → $S^+ + e^-$	0	2115
Si + FUV → $Si^+ + e^-$	14000	8350

[a] Derived from cross sections taken from Hollenbach & McKee 1979, 1989.

[b] From Gredel et al. 1989 with exception of the atoms that are estimated from above references.

© American Astronomical Society • Provided by the NASA Astrophysics Data System

1996ApJ...466..561M

1981; Black & van Dishoeck 1987; Gredel & Dalgarno 1995). We have incorporated the effects of nonthermal excitation on the H_2 vibration-rotation levels using the calculations of V91; we incorporate the effect of electronic excitations by assuming that the subsequent cascade through the vibration-rotation levels is the same as in the case of UV excitation in the low-density limit (i.e., no collisional de-excitation). Specifically, we assume that the quantity $I_{\rm line}/I_{\rm tot}$, the intensity in a particular line relative to the total intensity in near-infrared H_2 lines tabulated by Black & van Dishoeck (1987) for the UV-pumped case, gives the correct fraction of the total energy radiated in a particular line in the cascade following nonthermal excitation (in the absence of collisional de-excitation). We include a density-dependent term to suppress the cascade and nonthermal excitation contributions collisionally at densities above the critical densities.

2.1.4. *The Effect of X-Rays on Molecular and Atomic Species*

The incident X-ray flux affects the atomic and molecular chemistry not only through the ionization and heating due to secondary electrons but also via direct (primary) ionization. Although we assume secondaries dominate the ionization of H and He, we have included the direct ionization rates of C, O, S, Si, and Fe using the cross sections of Verner et al. (1993). X-ray ionization of molecules such as CO and OH will generally lead to their destruction. We assume that every primary ionization of a heavy element in a molecule leads to a doubly ionized species because of the Auger effect, which then dissociates into singly charged ions. For atomic carbon and oxygen, which are incorporated into the chemical network, we assume that X-ray ionization produces a singly charged ion. This is a reasonable assumption because any doubly charged ion will rapidly charge-exchange with hydrogen to produce a singly charged ion plus a proton; this is a very minor perturbation to the hydrogen ionization rate and can be ignored. For those species (Si, S, and Fe) that are not included in the chemical network, we assume that X-ray ionization produces a doubly charged ion and explicitly calculate the relative abundances of neutral, singly charged, and doubly charged atoms. Doubly charged species are never more than a minor fraction in the parameter space we consider.

Although most of the ionizations produced by a primary photoelectron are of H or H_2, the secondary ionizations of heavy elements may be significant in terms of the total heavy element ionization rate. To lowest order, the heavy element rates are just given by the hydrogen secondary ionization rate times the ratio of electron-impact ionization cross sections at the appropriate energy:

$$\zeta_{s,m} = \zeta_{s,\rm H} \frac{\sigma_{{\rm ei},m}(E)}{\sigma_{{\rm ei,H}}(E)} \ {\rm s}^{-1} \tag{10}$$

where the m subscript denotes a heavy element and $\sigma_{\rm ei}(E)$ is the electron-impact ionization cross section at energy E. Typically, E will be of the order of a few hundred eV for primary electrons and 50 eV for secondary electrons. These rates have been calculated using the analytic fits to experimental data of Lennon et al. (1988). A mean value for the energy range 0.1–1 keV is used for the cross section ratio; the dependence on energy of the actual ratio over this energy range is generally small (at most a factor of 2). Typically $\sigma_{{\rm ei},m}/\sigma_{{\rm ei},H} \sim 3$–7.

2.2. *Grain Heating and Cooling Mechanisms*

For the gas column densities that we consider, the grain opacity at FUV wavelengths is substantial, so that most of the FUV photons that are locally generated by the nonthermal electrons are absorbed by dust grains. This constitutes a significant heating source for the grains. We calculate the grain heating rate due to FUV photons under the assumption that all of the nonthermally generated FUV photons are locally absorbed. We also include the effect of FUV photons generated by radiative recombination, assuming 13.6 eV of photon energy per recombination.

At high densities, gas cooling via gas-grain collisions can become an important coolant, with the result that this also becomes an important heat source for the grains. Since comparable fractions of the deposited X-ray energy can go into gas heating and production of FUV photons, when gas-grain cooling is the dominant gas cooling mechanism, the grain heating rate will be approximately double the FUV heating rate. The gas-grain cooling rate is taken from Hollenbach & McKee (1989, hereafter HM89).

We calculate the equilibrium grain temperature under the assumption that the grains are optically thin to their own radiation, with a grain efficiency factor Q from Pollack et al. (1994). This simplified treatment is intended only to provide an estimate of the grain temperature and the infrared continuum radiated by the grains; in particular, we ignore the stochastic heating of small grains to high temperatures by absorption of X-ray photons (Voit 1991b).

The local FUV flux incident on the grains also provides another heating source for the gas, through FUV ejection of photoelectrons from the grains. We have ignored this process, however, as it is always of minor importance compared to the X-ray heating rate: although close to one-half of the total deposited X-ray energy may go into UV photons (at low ionization fractions), the efficiency of grain photoelectric heating of the gas is very low (0.1%–1%), so that at most $\sim$0.5% of the deposited X-ray energy goes into grain (FUV) photoelectric heating.

2.3. *Gas Cooling Mechanisms*

Over the range of X-ray fluxes and gas densities that we consider, the physical state of the gas ranges from warm and partially ionized ($T \sim 10^4$ K, $x_e \sim 0.01$–0.1) to cold and neutral ($T \sim 10$ K, $x_e \sim 10^{-6}$). Thus, a wide variety of species control the cooling, shifting in importance with X-ray flux and density.

At the highest temperatures, the gas cooling is dominated by collisional excitation of Lyα and forbidden and semiforbidden transitions of [O I] ($\lambda\lambda$6300, 6363), [C I] ($\lambda\lambda$9823, 9850), [Fe II] (1.26 and 1.64 μm), and [S II] ($\lambda\lambda$6716, 6731). Below $T \sim 5000$ K, the cooling is dominated by the fine-structure transitions of neutral and singly ionized atomic species such as [O I] (63 μm), [Si II] (35 μm), [C II] (158 μm), and [C I] (369 and 609 μm). All of the relevant atomic data for the atomic transitions have been taken from HM89, with the exception of [Fe II], for which we have used the calculations of Pradhan & Zhang (1993) and Zhang & Pradhan (1994). We include the effects of collisions with electrons, protons, and neutral and molecular hydrogen and the effects of radiative trapping.

We include cooling by the rotational and vibrational transitions of H_2, H_2O, and CO using the results of Neufeld & Kaufman (1993). Cooling by the rotational lines of OH has been included using the formalism of Hollenbach &

© American Astronomical Society • Provided by the NASA Astrophysics Data System

1996ApJ...466..561M

McKee (1979). The work of Neufeld & Kaufman and of Hollenbach & McKee does not include the effects of electron impact excitation; we have approximated the effects of electrons by using an appropriately scaled density, weighting the electron density using the results of Draine, Roberge, & Dalgarno (1983) and HM89 for H_2 and of Elitzur (1991, p. 207) for OH, CO, and H_2O. Electrons can be of more importance in X-ray–illuminated gas because of their higher abundance relative to normal molecular clouds or PDRs.

We calculate the cooling from H_2 collisional dissociation using the analytic expression for the dissociation rate coefficient and the rate in the high-density limit of Lepp & Shull (1983); the low-density coefficients are taken from HM89.

Gas-grain cooling is calculated using the expression of HM89; we assume that grains smaller than 10 Å have been destroyed by X-ray heating (Voit 1991b).

2.4. *Chemistry*

Our code solves for the equilibrium chemical abundances of 38 species of ions, atoms, and molecules, using a network of 157 chemical and radiative processes. The adopted abundances and standard parameters are given in Table 2. The hydrogen chemistry is the slowest chemistry to equilibrate, and the equilibrium timescale is set by the ionization rate of hydrogen, $t_{eq} \sim \zeta_T^{-1}$. In our typical example (the center of an $N_{cl} \sim 10^{22}$ cm^{-2} cloud at a distance of $r = 10^2 r_2$ pc from a $L = 10^{44} L_{44}$ ergs s^{-1} X-ray luminosity source), the equilibrium timescale becomes (from eq. [4])

$$t_{eq} \sim 3 \times 10^3 L_{44}^{-1} r_2^2 \text{ yr} . \quad (11)$$

This is much shorter than the dynamical time t_{dyn} for most cases considered (e.g., $t_{dyn} \sim 10^6 r_2/v_7$ yr for gas with velocity $v = 100 v_7$ km s^{-1}). Therefore, the simplifying assumption of equilibrium chemistry is generally justified.

Appendix B includes a complete list of the chemical reactions included in our code. Some of the key differences between this network and networks used for cold, opaque molecular cores include the enhanced X-ray ionization rates of various species, the dissociation and photoionization caused by the internally generated FUV photons, and the inclusion of neutral-neutral reactions with relatively high activation barriers that are overcome because of the elevated temperatures. We discuss below some of the main points involved in the chemistry of the major elemental families.

2.4.1. *Hydrogen Chemistry*

We have purposefully restricted the parameter space of H_X/n or ζ_T/n studied to include those regions in which these parameters are large enough to affect the chemistry significantly (e.g., dissociate H_2) and small enough that the gas is predominantly neutral. As a result, for most of our parameter range, the hydrogen is largely atomic but with significant (10^{-4} to 10^{-1}) concentrations of H_2 and H^+. The H_2 is largely formed on grain surfaces and by the reaction of H^- with H (see HM89 for adopted rates). The H_2 is largely destroyed by ionizing collisions with nonthermal secondary electrons produced by X-rays and by thermal dissociative collisions when the gas temperature exceeds $\sim$3000 K. The former process produces H_2^+ that generally reacts with H_2 to produce H_3^+. We have adopted the moderately fast electronic dissociative recombination rate for H_3^+ of Canosa et al. (1991); however, we find that our results are not sensitive to a significant reduction in this rate since H_3^+ also reacts rapidly with O, CO, OH, and H_2O. H^+ is produced by collisional ionization of H by nonthermal electrons and is destroyed by electronic recombination and by charge exchange reactions with O and CO. The charge exchange with O does not always lead to a net loss of H^+ since the reverse reaction is also fast. However, a fraction of the O^+ produced reacts with H_2 to form OH^+, thereby effectively destroying the H^+ ion.

TABLE 2

GAS-PHASE ABUNDANCES

Species	x_i[a]	δ_i[b]
He.....	0.1	1.0
O.....	5.0×10^{-4}	0.67
C.....	3.0×10^{-4}	0.67
Si.....	3.5×10^{-6}	0.09
Fe.....	1.0×10^{-6}	0.03
S.....	1.0×10^{-5}	0.52
Ni.....	1.0×10^{-7}	0.05

[a] Abundance relative to total hydrogen of element i.

[b] Depletion factor $\delta \equiv x_i$(Gas-phase)/x_i(Total).

2.4.2. *Ionization Balance and Electron Abundance*

One of the dominant reasons a numerical code is needed to solve the problem of X-ray–illuminated gas is the calculation of the electron abundance. As discussed in § 2.1.1, the electron abundance is an essential parameter that controls the heating rate and therefore the temperature of the X-ray–illuminated gas. The electron abundance is calculated from the balance of X-ray–induced ionization and electronic recombination with ions. This balance is sufficiently complicated to make analytic computation essentially impossible. The main complicating factors include the dependence of the recombination rates on temperature, the recombination of ions on small grains, and the large difference in the recombination rates of atomic ions as opposed to molecular ions. We amplify on the latter two complications below.

Draine & Sutin (1987) showed that ion recombination on grains becomes important when the electron fraction $x_e \lesssim 10^{-3}$ to 10^{-2} and that it is the smallest grains that dominate this process if a standard grain size distribution $n(a) \propto a^{-3.5}$ is assumed, where a is the grain radius. We have taken for our smallest grain size $a_{min} = 10$ Å, since Seyfert nuclei and quasars show none of the "PAH" infrared features identified with the 3–15 Å polycyclic aromatic hydrocarbons (Aitken & Roche 1985; Roche 1989) and, as noted earlier, dust grains smaller than 10 Å are expected to be rapidly destroyed by X-rays (Voit 1991b). (This cutoff size is not well determined, however, since it depends on the coupling between X-rays and PAHs, which is not well known.) We have then computed the fraction of these small grains that are singly positively charged, neutral, and singly negatively charged. Collisions with the neutral and negatively charged grains contribute to the recombination of atomic and molecular ions. Appendix C lists the grain reactions included and the rates adopted.

It is difficult to predict a priori (for example, from knowing the H_2 to H ratio) whether molecular ions or atomic ions dominate the recombination rate of electrons. We have discussed above how, in atomic gas, the H^+ can be channeled via O^+ to the molecular ion OH^+. Because of our inclusion of this channel and of the reactions of H_3^+

© American Astronomical Society • Provided by the NASA Astrophysics Data System

1996ApJ...466..561M

with oxygen species, we find electron fractions 10–100 times smaller than Krolik & Lepp (1989). The high electron fractions found in molecular gas in the latter paper result from the use of a slow H_3^+ recombination rate and the erroneous decoupling of the hydrogen chemistry from the heavy element chemistry (S. Lepp, private communication).

2.4.3. *Helium Chemistry*

The large abundance of helium means that a non-negligible fraction ($\approx 10\%$) of the secondary ionizations are of He (SvS85; V91). The presence of substantial amounts of He^+ has important consequences for the chemistry, as charge exchange reactions of the form $He^+ + MX \rightarrow He + M + X^+$ provide a rapid destruction mechanism for many species (e.g., CO). The presence of He^+ is also of interest in that HeH^+ has been suggested as a possible diagnostic of X-ray–illuminated neutral gas (Draine & Woods 1989). We calculate the HeH^+ abundance post facto using the radiative association rate of He^+ with H and the dissociative electronic recombination rate of HeH^+ from Cecchi-Pestellini & Dalgarno (1994).

2.4.4. *Oxygen Chemistry*

Atomic oxygen is converted to OH and H_2O via two basic routes. At low temperatures, $T \lesssim 300$ K, the charge exchange of H^+ with O produces O^+ that reacts with H_2 to form OH^+, H_2O^+, and H_3O^+. The OH^+ formed by this mechanism and by the reaction $H_3^+ + O \rightarrow OH^+ + H_2$ (which dominates at the lowest temperatures and ionization rates) is largely converted to H_2O^+ via $OH^+ + H_2 \rightarrow H_2O^+ + H$. The H_2O^+ and H_3O^+ ions produced by these reactions recombine with electrons to form OH and H_2O. These species are destroyed by reaction with O, C, and C^+ at low T. At high temperatures, neutral-neutral reactions with activation barriers dominate. O reacts with H_2 to form OH directly, and OH reacts with H_2 to form H_2O. O_2 is formed by the neutral-neutral reaction of OH with O. H_2O is destroyed primarily by the internally generated FUV and by high-temperature reactions with H atoms. In addition, reactions with vibrationally excited molecular hydrogen can be important.

2.4.5. *Carbon Chemistry*

The key reactions in producing CO are the reactions of C and C^+ with OH and H_2O. CO is destroyed primarily by charge exchange with He^+ and by the internally generated FUV photons. In atomic regions, C^+ is formed primarily by photoionization of C by X-rays and (as the molecular fraction increases) by photoionization of C by the FUV radiation field. In molecular (CO) regions, C^+ is produced largely by reaction of He^+ with CO. Therefore, carbon chemistry is primarily set by the internal FUV photons, the X-ray ionization of C and He, and the abundance of H_2 (which sets the OH and H_2O abundances).

3. MODEL PARAMETERS

As we noted earlier, the main parameter controlling the physical state of an X-ray–irradiated molecular cloud is the local X-ray energy deposition rate per particle divided by the gas density, H_X/n. We derive the relation of the local value of H_X/n to the X-ray flux incident on the cloud, the attenuating column, and the shape of the X-ray spectrum (assumed to be a power law) in Appendix A. Secondary parameters affecting the physical state are the total gas density n and, to a lesser extent, the total cloud column density N_c, as these affect, for example, the gas cooling rate through collisional de-excitation and radiative trapping. In modeling the effect of X-rays on a molecular cloud, we therefore have to make a specific choice as to the cloud column density and gas density. The results are also weakly dependent on the shape of the X-ray spectrum and on the cloud geometry (e.g., spherical or plane-parallel) as this affects the line escape probabilities.

Because the relative photoelectron energy loss routes are very weak functions of energy for photoelectron energies 100 eV $\lesssim E \lesssim$ 10 keV (SvS85; XM91; V91), the ionization, heating, and excitation rates due to secondary electrons, for a given H_X, are nearly independent of the incident X-ray spectrum. The primary ionization rates of the heavy elements do depend somewhat on the spectral shape, as the number of photons at a given photoionization threshold is the controlling parameter, rather than the energy absorbed. We will ordinarily assume a spectral index of 0.7 for the energy spectrum, the canonical observed value for the X-ray spectra of AGNs (Mushotzky et al. 1993). The most significant effect of changing the assumed spectral index is to alter the column density scaling of the local ionization and heating rates (Appendix A). The cloud column density and geometry also have minimal influence on the results for a given H_X/n.

For our general results we assume an X-ray flux that is normally incident on a cloud; the cloud size is assumed small compared to the distance to the X-ray source, so that geometric dilution of the flux across the cloud is negligible. We usually take the total column density through the cloud to be $N_c \sim 10^{22}$ cm^{-2}, comparable to the typical column densities through giant molecular clouds in the Galactic disk, and a line full width at half-maximum of 5 km s^{-1}. The attenuating column density N_{att} is generally set to be equal to or larger than the column density to cloud center, so that the gradients in the X-ray ionization and heating rates across the cloud are small. In calculating the escape probabilities we assume a plane-parallel geometry.

We have implicitly adopted the abundances of Morrison & McCammon (1983) for the total (gas-phase plus grain) abundances of our included species through our choice of X-ray cross section. Our adopted gas-phase abundances (relative to total H) are given in Table 2 and are essentially those of HM89. The corresponding elemental depletions are approximately those of van Steenberg & Shull (1988) and Jenkins (1989). We also assume a solar neighborhood dust-to-gas ratio, although we specifically allow for the change in grain surface area per H nucleus due to destruction of small grains by X-rays.

Models of optically thin X-ray–illuminated gas are characterized by the ionization parameter ξ, which is proportional to the ratio of photon flux to gas density or to H_X/n. This can be expressed in several different ways, e.g., $\xi = L_X/r^2 n = 4\pi F_X/n$ (Tarter, Tucker, & Salpeter 1969). We can write this as $\xi = 1.26 \times 10^{-4} F_X/n_5$, where the normally incident X-ray flux is F_X ergs cm^{-2} s^{-1}. From equations (2) and (3) and Appendix A, it is apparent that in our models, where the gas is optically thick to the X-rays below a maximum energy that depends on the column density, the relevant parameter is not the ionization parameter defined above but the effective (attenuated) ionization parameter, $\xi_{eff} = \xi/N_{att}^{\phi+1}$, where ϕ depends on the shape of the X-ray spectrum (Appendix A). Our nominal spectral index

© American Astronomical Society • Provided by the NASA Astrophysics Data System

1996ApJ...466..561M

$\alpha = 0.7$, and so

$$\xi_{\rm eff} \equiv \frac{\xi}{N_{22}^{0.9}} = 1.26 \times 10^{-4} \frac{F_x}{n_5 N_{22}^{0.9}} \quad (12)$$

(recall that $N_{22} = N_{\rm att}/10^{22}$ cm^{-2}). Note that $\xi_{\rm eff}$ is directly proportional to $H_{\rm X}/n$; for $\alpha = 0.7$,

$$H_{\rm X} = 4.8 \times 10^{-24} \frac{F_{\rm X}}{N_{22}^{0.9}} \text{ ergs s}^{-1} \quad (13)$$

or, alternatively,

$$H_{\rm X}/n = 3.8 \times 10^{-25} \xi_{\rm eff} \text{ ergs s}^{-1} . \quad (14)$$

Because of our assumption that secondary ionizations always dominate the total hydrogen ionization rate, our results cannot be extrapolated below $N_{22} \sim 0.01$. We present our model results in terms of both $H_{\rm X}/n$ and $\xi_{\rm eff}$; we have calculated results for $\xi_{\rm eff} = 10^{-5}$ to 1, or equivalently $H_{\rm X}/n = 3.8 \times 10^{-30}$ to 3.8×10^{-25} ergs cm^3 s^{-1}. In the following section, we present analytic and numerical results (chemistry, ionization, temperature, and line intensities) for our standard cloud parameters for gas densities of 10^5 and 10^3 cm^{-3}, chosen to span the range of densities of normal molecular clouds. (Results for clouds at very high pressures, as expected in obscuring "tori" around AGNs, will be presented in a subsequent paper [Maloney, Hollenbach, & Tielens 1996]; see also Maloney, Begelman, & Rees 1994; Neufeld, Maloney, & Conger 1994; and Maloney 1996.) In addition, we show the chemical and thermal structure as a function of depth into a cloud for a density of 10^5 cm^{-3}; these depth-dependent models verify our assertion that the major parameter governing the physical conditions in X-ray–illuminated gas is $H_{\rm X}/n$ or, equivalently, $\xi_{\rm eff}$.

4. RESULTS

As we noted earlier, solving for the chemical, thermal, and ionization structure of an X-ray–irradiated parcel of dense gas in general requires the solution of a large set of coupled equations. However, it is possible to make useful analytic estimates of some important parameters. We do this in the following section; in § 4.2 we present numerical results for our standard cloud models, and in § 4.3 we present models showing specifically the depth-dependence of the temperature, ionization fraction, and abundances of the major species.

4.1. *Analytic Estimates*

The molecular hydrogen ionization rate (per *molecule*) is given by (from eqs. [3] and [14])

$$\zeta_{\rm H_2} = 3.0 \times 10^{-9} f_i n_5 \xi_{\rm eff} \text{ s}^{-1} , \quad (15)$$

where f_i ($\sim$0.4) is the fraction of primary photoelectron energy that goes into ionization. We approximate the atomic hydrogen rate by $\zeta_{\rm H} \approx (15.4/13.6) \times 0.5\zeta_{\rm H_2}$ (correcting for the difference in ionization energies; when the ionization fraction is small, the fraction of primary electron energy that goes into ionization is very similar for atomic and molecular gas, and the H and H_2 ionization rates are related by this simple expression to reasonable accuracy; cf. § 2.1). Similarly, the gas heating rate (per unit volume) is

$$n\Gamma_{\rm X} = 3.8 \times 10^{-15} f_h n_5^2 \xi_{\rm eff} \text{ ergs cm}^{-3} \text{ s}^{-1} , \quad (16)$$

where f_h ($\sim$0.3) is the fraction of the absorbed X-ray energy that goes into gas heating (see Appendix A). We will use these approximations to the ionization and heating rates to derive approximate expressions for the abundances of electrons and H_2 and for the value of the ionization parameter at which luminous molecular hydrogen vibration-rotation emission is produced.

Consider first the electron abundance. When $\xi_{\rm eff} \gg 1$, the gas is highly ionized; we do not treat this case in this paper. When $10^{-3} \ll \xi_{\rm eff} \lesssim 1$, the gas is primarily atomic, and the electron fraction is set by the balance between X-ray ionization and radiative recombination of H^+. Approximating the recombination coefficient by $\alpha_B \approx 1.3 \times 10^{-12} T_3^{-0.7}$, and assuming that $x_e \ll 1$, equation (15) gives the result

$$x_e \approx 0.12 \xi_{\rm eff}^{1/2} T_3^{0.35} f_i^{1/2} ; \quad 10^{-3} \ll \xi_{\rm eff} \lesssim 1 . \quad (17)$$

At low T and increasing molecular abundances, additional electron recombination mechanisms, such as dissociative recombination, become important. For example, at 2000 K, electron destruction via dissociative recombination of OH^+ is competitive with radiative recombination of H^+, and the electron fraction is reduced by a factor of 1.5 from equation (17). Even relatively small molecular ion abundances can affect the electron abundance because of the vastly higher rate coefficient for dissociative recombination (typically $\sim 10^{-7}$ cm^3 s^{-1}) compared with radiative recombination ($\sim 10^{-12}$ cm^3 s^{-1}). When the ionization parameter is sufficiently small ($\xi_{\rm eff} \ll 10^{-3}$) that the gas is largely molecular (see below), the electron fraction is given by an expression similar to equation (17), but the numerical coefficient is smaller by a factor of $\sim (10^5)^{1/2}$, reflecting the much higher rate coefficient for dissociative recombination:

$$x_e \approx 3 \times 10^{-4} \xi_{\rm eff}^{1/2} T_3^{1/2} f_i^{1/2} ; \quad \xi_{\rm eff} \ll 10^{-3} . \quad (18)$$

An analytic estimate of the H_2 abundance requires knowledge of the formation and destruction paths. The nature of the molecular hydrogen destruction mechanisms depends on the abundances of molecules. When the molecular hydrogen fraction is large, the destruction of H_2 is initiated primarily by X-ray ionization. Each H_2 or H ionization leads to the destruction of typically three H_2 molecules, as the ions react in the ion-molecule chemistry. Therefore, equating the H_2 destruction rate to the formation rate on grains, we obtain the following approximate expression for the H_2 to H ratio for relatively large molecular abundances:

$$\frac{n_{\rm H_2}}{n_{\rm H}} = 1.1 \times 10^{-4} \frac{R_{-17}}{f_i \xi_{\rm eff}} ; \quad \xi_{\rm eff} \lesssim 10^{-3} \quad (19)$$

where R_{-17} is the molecular hydrogen grain formation coefficient $R_f/10^{-17}$ cm^3 s^{-1}. Assuming $R_{-17} = 3$, equation (19) predicts that the gas is half-molecular ($n_{\rm H_2}/n_{\rm H} = 1/2$) at $\xi_{\rm eff} = 1.7 \times 10^{-3}$ (assuming $f_i \approx 0.4$). The actual value is $\xi_{\rm eff} \approx 1.4 \times 10^{-3}$ for $n = 10^5$ cm^{-3}.

When the gas is largely atomic ($\xi_{\rm eff} \gg 10^{-3}$), the nature of the H_2 equilibrium is qualitatively different: destruction by X-ray ionization is unimportant, and H_2 is destroyed largely by reaction with O^+:

$$O^+ + H_2 \rightarrow OH^+ + H . \quad (20)$$

(As the temperature increases above $T \sim 3000$ K, reaction of H_2 with neutral oxygen also becomes important.) The abundance of O^+ is determined by its very rapid charge exchange with H, so that $O^+/O \simeq H^+/H$. If we equate

© American Astronomical Society • Provided by the NASA Astrophysics Data System

1996ApJ...466..561M

destruction by reaction (20) with the formation rate and use (17) to estimate the H^+ abundance, we obtain an equilibrium molecular hydrogen abundance

$$x_{H_2} = 5.4 \times 10^{-8} R_{-17} x_O^{-1} (\xi_{eff} T_3^{0.7} f_i)^{-1/2} ; \quad (21)$$

recall that our adopted gas-phase oxygen abundance $x_O = 5 \times 10^{-4}$. Comparison with the numerical results shows that this expression is accurate to better than a factor of 2 for $T = 1500$–3500 K at $n = 10^5$ cm^{-3}.

We would like to be able to make a self-consistent *analytic* estimate of the temperature as a function of ionization parameter ξ_{eff} for the above T range, where vibrationally excited molecular hydrogen emission can be important. Optically thin thermally excited H_2 emission is the dominant coolant. An excellent fit to the cooling rate coefficient for collisions with atomic hydrogen is (for $n = 10^5$ cm^{-3})

$$L_{vr}(H_2) = 9.6 \times 10^{-24} e^{-7.01/T_3} \text{ ergs cm}^3 \text{ s}^{-1} , \quad (22)$$

where the cooling rate per unit volume $n^2 \Lambda_{vr} \equiv n^2 x_{H_2} L_{vr}$. This fits our adopted rates to 2% or better from $T = 500$ to 3500 K. For $n > 10^5$ cm^{-3}, the cooling rate coefficient will decrease approximately as n_5^{-1}; for $n < 10^5$ cm^{-3}, there is little density dependence. Equating this cooling rate to the heating rate (16), we obtain the approximate solution

$$T_3 = 7.01[-13.5 - \ln(f_h \xi_{eff}^{3/2} f_i^{1/2} x_O / R_{-17})]^{-1} ; \quad (23)$$

where we have used equation (21) for the molecular hydrogen abundance (but ignored the weak temperature dependence of this quantity). Equation (23) predicts that the temperature will be 2000 K (i.e., that the vibration-rotation bands of H_2 will be excited) at $\xi_{eff} = 2.7 \times 10^{-2}$. Thus we expect that molecular hydrogen vibrational emission will be important for values of $\xi_{eff} \approx$ few $\times 10^{-2}$; this is confirmed by our detailed numerical results (see below). We note that although H_2 2 μm emission is a powerful coolant at these values of ξ_{eff}, the fractional abundance of H_2 is not high, with $x_{H_2} \sim 10^{-3}$.

4.2. *Numerical Results*

4.2.1. *Thermal, Chemical, and Ionization State*

Figure 3*a* shows the temperature and the abundances of major molecular and atomic species in the XDR as a function of ξ_{eff} and H_X/n for a total hydrogen density $n = 10^5$ cm^{-3}. At the highest values of H_X/n or ξ_{eff}, the gas is atomic ($x_{H_2} < 10^{-5}$), warm ($T \approx 10^4$ K), and partially ionized ($x_e \approx 0.1$). With decreasing X-ray ionization and heating (decreasing H_X/n and ξ_{eff}) the temperature and ionization fraction slowly decline, while the molecular abundances increase. This behavior continues until H_X/n drops to 2×10^{-26} ($\xi_{eff} \approx 4 \times 10^{-2}$) at which point the gas temperature drops much more rapidly to $T \approx 3000$ K. The abundance of molecular hydrogen increases by an order of magnitude in this transition region, as the temperature drop produces a concomitant decrease in the rate of collisional dissociation and of H_2-destroying neutral-neutral reactions; the abundances of the other major molecular species (e.g., CO and OH) increase by comparable factors.

Beyond this transition point, the abundances of OH and (especially) CO actually decline slightly with decreasing ξ_{eff}, in consequence of the continuing temperature drop, which reduces the rates of OH- and CO-forming neutral-neutral reactions with activation energy barriers. (The gas temperature $T = 2000$ K at $\xi_{eff} \approx 2.3 \times 10^{-2}$, in good agreement with eq. [23].) After H_X/n and ξ_{eff} have dropped by another factor of a few, however, and the temperature has dropped to $T \sim 700$ K, this effect is outweighed by the rapid increase in the abundance of H_2 and the molecular ion H_3^+, which drive the ion-molecule chemistry (see below). At the lowest values of H_X/n and ξ_{eff}, less than 1% of the hydrogen is atomic, the electron fraction $x_e \approx 10^{-6}$, the temperature $T \approx 25$ K, and virtually all of the gas-phase carbon is in CO. Much of the gas-phase oxygen is still atomic; the abundances of the other important O-containing molecules such as OH, O_2 and H_2O are typically 10^{-6} to 10^{-5}. This is very similar to the physical conditions in the opaque cores of cosmic-ray–irradiated molecular clouds in the solar vicinity.

Figure 3*b* plots the same quantities as Figure 3*a*, only for $n = 10^3$ cm^{-3}; the total column and line width are the same. Qualitatively the results are very similar to the $n = 10^5$ cm^{-3} model (confirming the prediction that H_X/n is the dominant controlling parameter), although there are some quantitative differences due to density-dependent

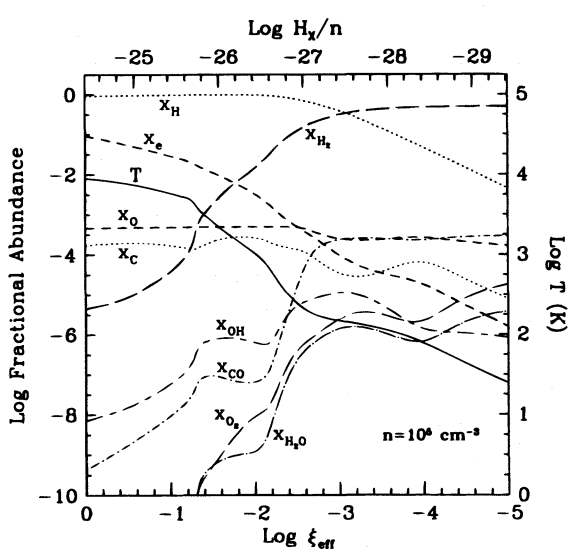

FIG. 3*a*

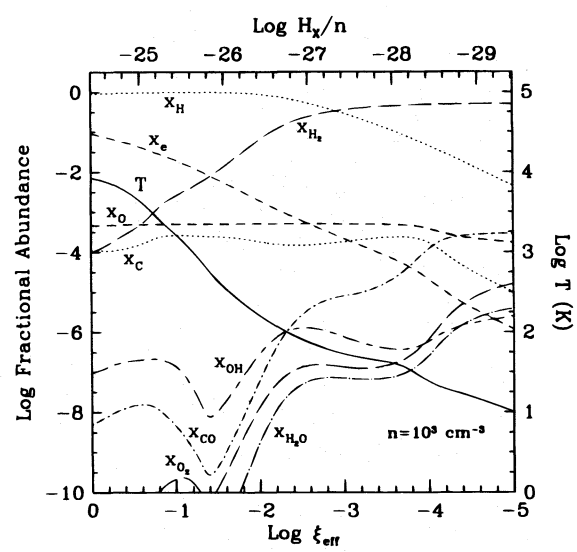

FIG. 3*b*

FIG. 3.—Temperature and major species abundances in an XDR as a function of the effective ionization parameter ξ_{eff}, or, equivalently, H_X/n. The right-hand axis is the temperature scale, and the left-hand axis is the abundance scale. (*a*) Total hydrogen density $n = 10^5$ cm^{-3}. (*b*) $n = 10^3$ cm^{-3}.

© American Astronomical Society • Provided by the NASA Astrophysics Data System

1996ApJ...466..561M

quantities (e.g., line cooling). The most significant difference between the two models is that the rather steep change in temperature and molecular abundances at $\xi_{\rm eff} \approx 4 \times 10^{-2}$ visible in Figure 3*a* has disappeared; the temperature simply drops steadily with H_X/n and $\xi_{\rm eff}$ and is in general lower than in the $n = 10^5$ cm^{-3} model. This is again a consequence of the much lower densities; in particular, cooling by the pure rotational and vibration-rotation lines of H_2 is collisionally suppressed at high density and is relatively much more important in the low-density model. Molecular hydrogen becomes dominant at about the same value of H_X/n or $\xi_{\rm eff}$ in both models, but the rise in the abundances of molecules such as CO and OH is slower in the $n = 10^3$ cm^{-3} model, which reflects the lower temperatures that reduce the formation rates of these molecules, and the initial dip in molecular abundances with decreasing temperature is much more pronounced. At the lowest ionization parameters, the results are essentially identical: the gas is almost entirely molecular, the ionization fraction is small, and nearly all of the gas-phase carbon is in CO.

The ion chemistry is important since the electron fraction directly influences the heating and ionization rates. In Figure 4*a* we have plotted the important ionic species as a function of $\xi_{\rm eff}$ and H_X/n for $n = 10^5$ cm^{-3}. H^+ is the dominant ion in atomic gas ($\xi_{\rm eff} \gg 10^{-3}$). In molecular gas ($x_{H_2} > x_H$, $\xi_{\rm eff} < 10^{-3}$) C^+ is the major ion; singly ionized carbon is produced mainly by UV photoionization of neutral carbon and by dissociation following charge exchange of He^+ with CO. O^+ is much less abundant largely because singly ionized oxygen is far more reactive than C^+; in particular, it reacts readily with H_2 to produce OH^+ (eq. [20]). At the lowest values of $\xi_{\rm eff}$ that we consider the H_3^+ ion is nearly as abundant as C^+, and Si^+ and S^+ can also be important.

Particularly noticeable in the ion chemistry in Figure 4*a* is the very rapid rise of the H_3^+ abundance with decreasing $\xi_{\rm eff}$ or H_X/n beyond the temperature drop/molecular abundance increase discussed above, at $\xi_{\rm eff} \approx 4 \times 10^{-2}$. At the start of this transition region, H_2^+ is roughly 3 orders of magnitude more abundant than H_3^+, but $x_{H_3^+}$ increases much more rapidly and exceeds H_2^+ in abundance by the time $\xi_{\rm eff}$ has dropped about an order of magnitude. This behavior can be simply understood from the hydrogen chemistry. H_3^+ is formed by the reaction (5a) between H_2^+ and H_2 and is thus proportional to $x_{H_2} x_{H_2^+}$. As long as reaction (5a) is not also the primary destruction mechanism for H_2^+ (i.e., as long as dissociative recombination or charge exchange with H dominate), then the H_2^+ abundance is also proportional to x_{H_2}, and so the abundance of $H_3^+ \propto x_{H_2}^2$. Since the molecular hydrogen abundance itself is increasing faster than $\xi_{\rm eff}^{-1}$ in this portion of parameter space, the result is a very rapid increase in $x_{H_3^+}$ with decreasing $\xi_{\rm eff}$. Once reaction (5a) becomes the major loss route for H_2^+, this scaling breaks down: when the gas is largely molecular (low H_X/n and $\xi_{\rm eff}$), the H_3^+ abundance is set by the balance between formation via reaction (5a) and destruction mostly by electronic recombination. In this limit, $x_{H_3^+}$ tends to a relatively constant value, set by the ratio of H_2 ionization rate to electron density.

The behavior of the ionic abundances for $n = 10^3$ cm^{-3}, shown in Figure 4*b*, is very similar; although there are some quantitative differences, the major transitions (e.g., the dominance of H_3^+ over H_2^+, or C^+ over H^+) occur at approximately the same values of ionization parameter.

4.2.2. *Gas Cooling*

In Figure 5 we have plotted both the total gas cooling (ergs cm^{-3} s^{-1}) and the major coolants as a function of H_X/n and $\xi_{\rm eff}$ for $n = 10^5$ cm^{-3}. (For optically thick coolants, the effective emissivity, including the effects of radiative trapping, is plotted.) As noted earlier, over our range of parameter space for XDRs, the temperature ranges from $T \approx 10^4$ K to $T \approx 10$ K, so that a wide range of atomic and molecular species contribute to the cooling. The transition from warm atomic to cold molecular gas is clearly delineated by the shift from atomic to molecular and gas-grain cooling with decreasing $\xi_{\rm eff}$. The dominant coolant shifts from Lyα, [O I] λ6300, and [C I] $\lambda\lambda$9823, 9850 at the highest temperatures to the H_2 vibration-rotation lines, the [O I] 63 μm line, and then to CO rotational cooling, as H_X/n declines. At the lowest ionization parameters and temperatures, gas-grain cooling becomes the single most important gas-phase cooling mechanism. We note that the [O I]

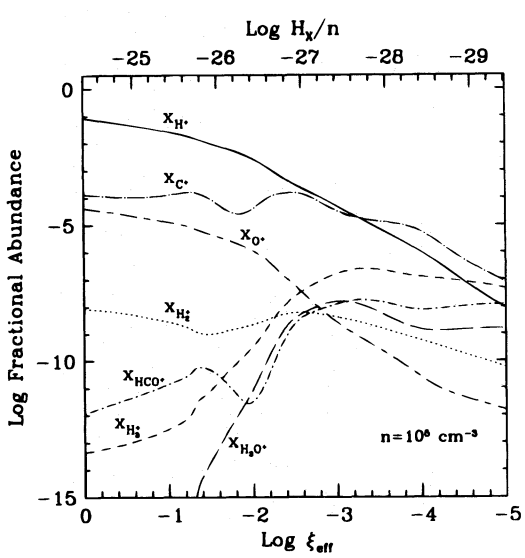

FIG. 4*a*

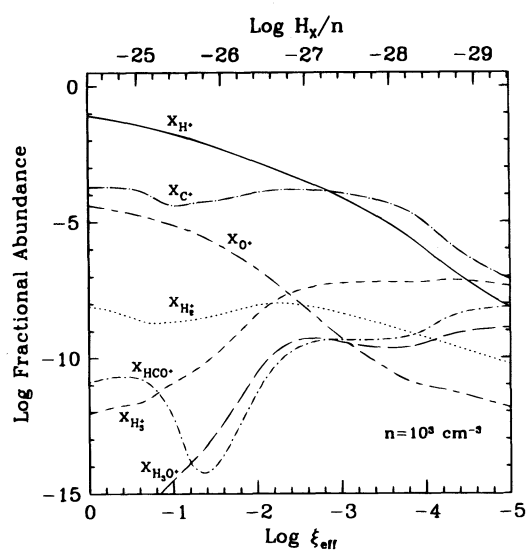

FIG. 4*b*

FIG. 4.—Abundances of major ionic species as a function of $\xi_{\rm eff}$ and H_X/n. (*a*) $n = 10^5$ cm^{-3}. (*b*) $n = 10^3$ cm^{-3}.

© American Astronomical Society • Provided by the NASA Astrophysics Data System

1996ApJ...466..561M

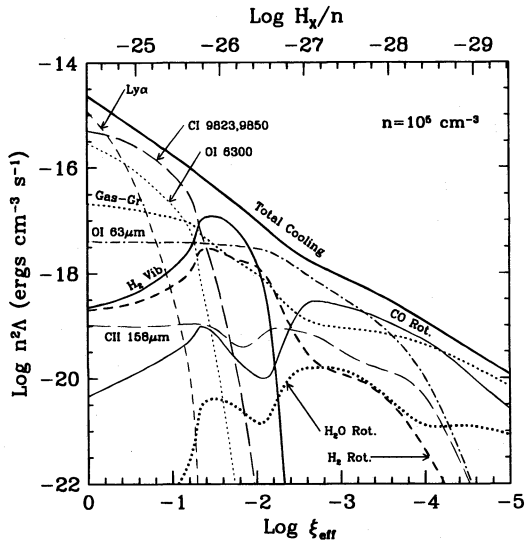

FIG. 5.—Total cooling rate and major coolants as a function of ξ_{eff} and H_X/n, for $n = 10^5$ cm^{-3}. For optically thick species, the effective emissivity, including the effects of radiative trapping, is plotted.

63 μm fine-structure line is a major coolant throughout a large portion of the modeled parameter space.

4.2.3. *Line and Continuum Emission*

The wide range of important coolants as a function of H_X/n or ξ_{eff} also means that there is a large number of important diagnostic emission lines from XDRs. Of particular interest are potentially observable near-, mid-, and far-infrared transitions.

The results plotted in Figures 3–5 are relatively insensitive to the column density of 10^{22} cm^{-2} chosen for our specific models. This is because a significant column density dependence for the local parameters arises only when the dominant coolants become optically thick, and as Figure 5 demonstrates, effectively optically thin coolants such as Lyα, [O I] λ6300, [C I] λλ9823, 9850, H_2 vibration and rotation lines, and gas-grain collisions either dominate or are comparable to the optically thick coolants such as [O I] 63 μm and CO rotational lines. However, the most useful parameter for comparison with observations is the emergent intensity from a cloud. We will approximate the emergent intensity by plotting an intensity I/N_{22} given by

$$\frac{I}{N_{22}} = \frac{10^{22}\ \mathrm{cm}^{-2}\ n\Lambda_l}{4\pi}, \tag{24}$$

where $n\Lambda_l$ is the cooling rate per particle in line l, calculated at a column of 10^{22} cm^{-2}. I is approximate for a column of 10^{22} because the implicit assumption is that $n\Lambda_l$ does not depend on column within the cloud. Although, as argued above, many cooling rates are relatively insensitive to the column for *fixed heating* (i.e., H_X/n), the heating rate will also vary somewhat with column in the cloud, as we discuss below in § 4.3. I is somewhat more approximate for clouds with total columns differing from 10^{22} cm^{-2}, since we compute Λ_l using an absorbing column of 10^{22} cm^{-2}. However, to first order, the optically thin intensities will scale linearly with N for small excursions from 10^{22} cm^{-2}. Optically thick lines will be relatively independent of N.

Figure 6*a* shows the standard cloud emergent integrated intensities of 4 of the most commonly observed near-infrared transitions: Brγ at 2.17 μm, the $v = 1$–0 $S(1)$ and $v = 2$–1 $S(1)$ lines of molecular hydrogen at 2.1218 μm and 2.248 μm, respectively, and the [Fe II] transition at 1.64 μm. Aside from Brγ, which shows an essentially monotonic decrease with H_X/n (reflecting chiefly the drop in ionization fraction), these transitions show very structured behavior with ionization parameter. The [Fe II] 1.64 μm line is bright interior to the temperature decrease at $\xi_{eff} \sim 4 \times 10^{-2}$ and then drops dramatically in intensity. This results largely from the temperature drop: since the upper state of the 1.64 μm line (and the 1.26 μm line, which shows identical behavior) lies about 10^4 K above the ground, the gas temperature must be at least $T \approx 3000$–4000 K in order to excite it collisionally. For ionization parameters $\xi_{eff} \gtrsim 4 \times 10^{-4}$, most of the iron is maintained as Fe^+ by photoionization by the locally generated UV photons, so that the [Fe II] line intensities scale directly with the gas-phase Fe abundance.

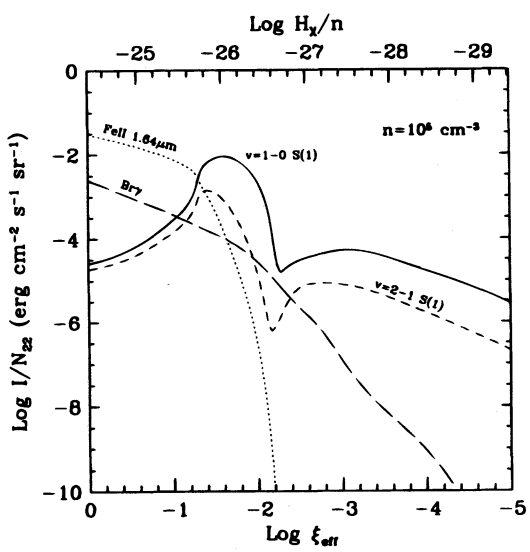

FIG. 6*a*

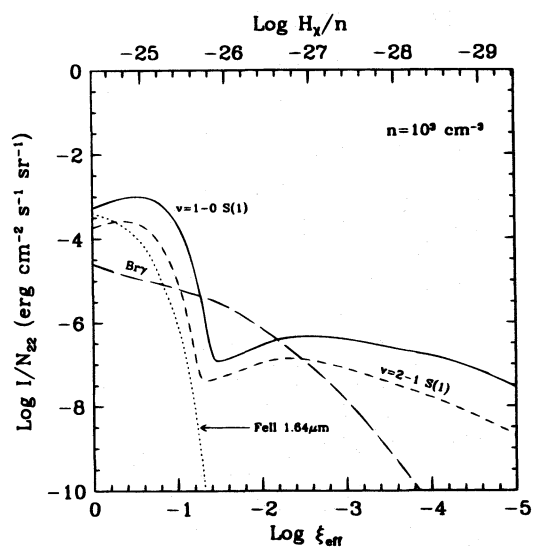

FIG. 6*b*

FIG. 6.—Emergent integrated intensities from a cloud of column density 10^{22} cm^{-2} in the [Fe II] 1.64 μm line, Brγ, and the $v = 1$–0 and $v = 2$–1 $S(1)$ lines of molecular hydrogen, as a function of ξ_{eff} and H_X/n. (*a*) $n = 10^5$ cm^{-3}. (*b*) $n = 10^3$ cm^{-3}.

© American Astronomical Society • Provided by the NASA Astrophysics Data System

1996ApJ...466..561M

The vibration-rotation transitions of H_2 increase slowly with decreasing H_X/n, as the H_2 abundance increases, and then rise steeply at $\xi_{eff} \sim 4 \times 10^{-2}$, reflecting the rapid increase in x_{H_2}. Since even the lowest J levels in $v = 1$ and $v = 2$ lie approximately 6000 K and 12,000 K above ground, respectively, the intensity of emission in the $v = 1$–0 $S(1)$ line drops rapidly once the temperature decreases below about 1500 K, while the intensity of the $v = 2$–1 $S(1)$ begins declining immediately as ξ_{eff} decreases. In agreement with the analytic estimate of § 4.1, the vibration-rotation transitions of H_2 peak at $\xi_{eff} \approx$ few $\times 10^{-2}$. Both line intensities reach a minimum and then rise again to a broad peak, followed by a slow decline. This secondary rise is produced by excitations of the $v = 1$ and $v = 2$ levels by the fast nonthermal electrons, either directly from $v = 0$ or by cascade following excitation to a higher electronic state (V91; Gredel & Dalgarno 1995). The fraction of nonthermal electron energy that goes into excitations of H_2 increases as the ionization fraction drops; the slow drop-off in intensity with further decrease in ξ_{eff} is simply due to the decrease in X-ray energy deposition. Note also that the intensity of the $v = 2$–1 line increases relative to the $v = 1$–0 line as the nonthermal excitations become dominant. This behavior results from the fact that the nonthermal excitations become more important than the thermal excitation rates (which are dominated by collisions with atomic hydrogen) only when the temperature drops below about 500 K, so that the ratio of the $v = 2$–1 to $v = 1$–0 line corresponds to this temperature at the minimum. When nonthermal direct excitation dominates, however, the $v = 2$–1 to $v = 1$–0 line ratio depends only on the ratio of the cross sections for excitation by the electrons to $v = 1$ and $v = 2$; this ratio corresponds to a temperature $T \approx 1700$ K, as noted in § 2.1.3. When cascade following electronic excitation dominates, the line ratio can be as high as 0.54, corresponding to a temperature $T \approx 3500$ K. Thus, the $v = 2$–1 $S(1)/v = 1$–0 $S(1)$ line ratio increases when the nonthermal excitations become dominant. The ratio then decreases somewhat with further decrease in ξ_{eff}, as the cascade contribution becomes less important relative to direct excitation to $v = 1$ and $v = 2$, in consequence of the continuing decline in electron fraction. Our results are in good agreement with the recent detailed treatment of excitation by nonthermal electrons of Gredel & Dalgarno (1995).

The major point from Figure 6*a* is that the emergent intensities in all these lines are extremely high, peaking at $\sim 10^{-2}$ ergs cm^{-2} s^{-1} sr^{-1}. The Brγ and [Fe II] lines peak interior to (at higher ξ_{eff} than) the molecular hydrogen lines.

Figure 6*b* shows the same transitions for the $n = 10^3$ cm^{-3} case. Aside from the more gradual nature of the atomic to molecular transition noted earlier, the behavior is qualitatively similar to the standard case. The chief difference, aside from the generally lower integrated intensities, is that the [Fe II] emission does not exceed the $v = 1$–0 line even at the highest values of ξ_{eff}, as the molecular hydrogen emission peak is broader and occurs at a smaller ξ_{eff} compared to the $n = 10^5$ cm^{-3} case.

In Figure 7*a*, we plot the total integrated intensities in pure rotational lines for the H_2, CO, OH, and H_2O molecules, plus the total vibrational lines of H_2. (Note that we plot only the thermal contribution to the H_2 emission and not the nonthermal excitations discussed above.) Also plotted is the total infrared emission from grains. The fact that the total luminosities in, e.g., the H_2 vibrational and CO rotational lines (over different ranges of ionization parameter) are a major fraction of the total infrared emission from grains indicates that individual lines [such as the $v = 1$–0 $S(1)$ line] from XDRs can have very large line fluxes relative to the bolometric IR flux, much larger than in PDRs. Figure 7*b* shows the same results for the $n = 10^3$ cm^{-3} case; the major difference from the standard density case is that the pure rotational lines of H_2 are relatively more important, as the density is well below the critical density for the vibrational lines but not for the pure rotation lines.

A large number of mid- and far-infrared atomic fine-structure lines from neutral or singly ionized species are produced in XDRs. Figure 8*a* shows a number of the most important transitions for $n = 10^5$ cm^{-3}. The single most important line at $n = 10^5$ cm^{-3} is the [O I] 63 μm line,

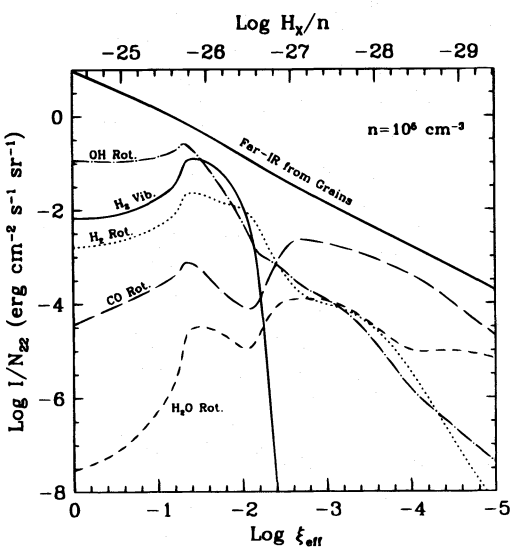

FIG. 7*a*

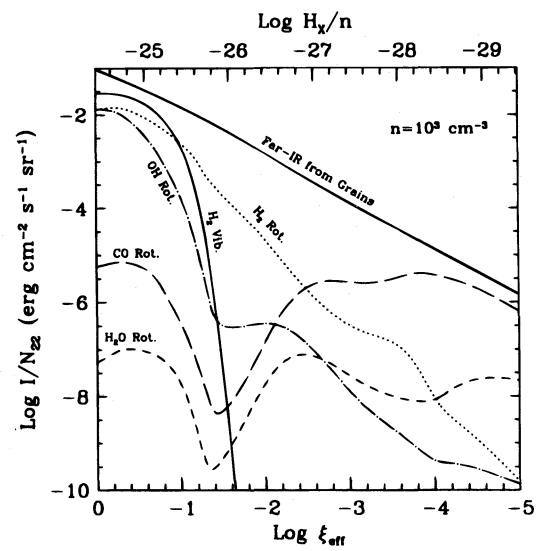

FIG. 7*b*

FIG. 7.—Total emergent integrated intensities from a cloud of column density 10^{22} cm^{-2} in the rotational lines of CO, OH, H_2, and H_2O and the vibration-rotation lines of H_2, as a function of ξ_{eff} and H_X/n. Also plotted is the estimated total far-infrared emission from dust grains. (*a*) $n = 10^5$ cm^{-3}. (*b*) $n = 10^3$ cm^{-3}.

© American Astronomical Society • Provided by the NASA Astrophysics Data System

1996ApJ...466..561M

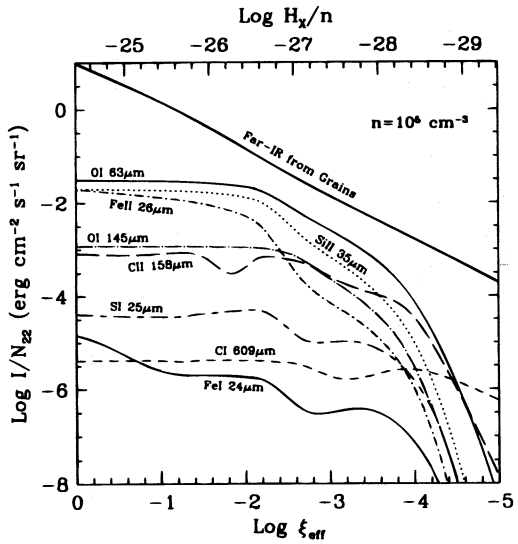

FIG. 8*a*

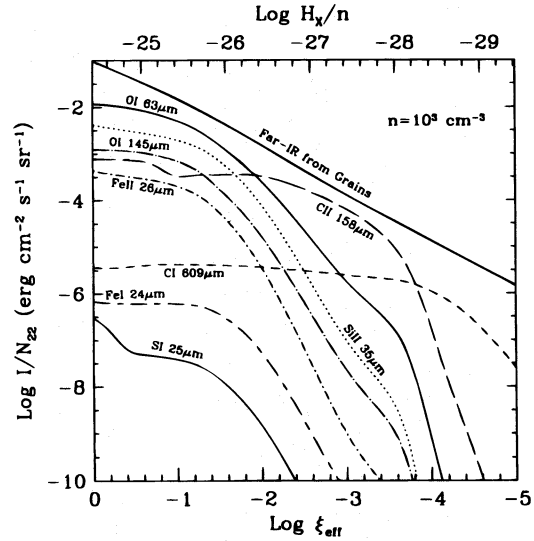

FIG. 8*b*

FIG. 8.—Mid- and far-infrared fine-structure emission line integrated intensities from a cloud of column density 10^{22} cm^{-2}, as a function of ξ_{eff} and H_x/n. Also plotted is the estimated total far-infrared emission from dust grains. (*a*) $n = 10^5$ cm^{-3}. (*b*) $n = 10^3$ cm^{-3}. Note that individual lines such as [O I] 63 μm and [C II] 158 μm can reach a significant fraction ($\sim$0.1) of the infrared grain continuum.

which, as noted earlier, is a major gas coolant over most of the calculated range of H_X/n and ξ_{eff}. As above, the large ratio of the integrated intensity in this line to the total IR continuum from grains indicates that the line–to–total continuum ratio for the 63 μm line can be very large, in excess of 10%. The [Si II] 35 μm, [Fe II] 26 μm, and [C II] 158 μm lines are also very bright over different ranges of ionization parameter. Just as is the case for the near-IR lines plotted in Figure 7, the integrated intensities are very large, $\sim 10^{-3}$ to 10^{-2} ergs cm^{-2} s^{-1} or more for the brightest lines. Figure 8*b* shows the same lines for the $n = 10^3$ cm^{-3} model; the most noticeable differences are the greater relative importance of the [O I] 145 μm line and, especially, the [C II] 158 μm line, due to the lower density and temperatures in the $n = 10^3$ cm^{-3} model. (The intensity of the [O I] 63 μm line decreases rapidly with decreasing T and n.) The 158 μm line is by far the brightest line over a substantial range (about two decades) in ionization parameter at this density.

4.2.4. H_3^+, HeH^+, *and* H_3O^+ *Emission*

As noted in § 2.4.3, the presence of detectable levels of HeH^+ has been suggested as a possible diagnostic of X-ray–illuminated neutral gas (Draine & Woods 1989), as has emission from H_3^+ (Draine & Woods 1990, although note that this is a time-dependent calculation). Here we briefly discuss the expected intensity of emission from these species. In addition, in our models H_3O^+ is often comparable in abundance to H_3^+, and so we estimate the intensity of H_3O^+ emission as well.

We have estimated the intensity of the HeH^+ 149 μm rotation line and the 3.364 and 3.608 μm rovibrational lines following Cecchi-Pestellini & Dalgarno (1993). Typically, the HeH^+ abundance is small, $\sim 10^{-10}$ to 10^{-9}. The resulting intensities are plotted in Figure 9*a* (for $n = 10^5$ cm^{-3}) and Figure 9*b* ($n = 10^3$ cm^{-3}). (Note that the plotted curve for the rovibrational transitions applies to either line, not the sum.) From Figure 9 it is clear that in the higher density model, both the 149 μm rotational line and the rovibrational lines are bright enough to be potentially detectable; for extragalactic sources, the 3.364 and 3.608 μm lines would clearly be preferable as beam dilution will be much less severe. At $n = 10^3$ cm^{-3}, the surface brightnesses are much lower and will generally not be observable.

We have also estimated the intensities of the H_3O^+ 364 and 396 GHz transitions, following Phillips, van Dishoeck, & Keene (1992), and of the vibrational transitions around 4 μm of H_3^+, following Draine & Woods (1990). The estimated intensities for these lines are also shown in Figures 9*a* and 9*b*. In all cases, these lines are prohibitively faint.

4.3. *Depth-dependent Models*

The numerical results discussed in § 4.2 assume a fixed attenuating column density and cloud column; H_X/n and ξ_{eff} are varied by varying the incident flux. Here we present results for the depth dependence of the temperature, ionization fraction, and major species abundances. In this case the incident flux is fixed, but H_X/n and ξ_{eff} decrease because of the attenuation of the X-rays by absorption with depth into the cloud (cf. the discussion before eq. [13]). The total hydrogen density is 10^5 cm^{-3}; the initial attenuating column is 10^{21} cm^{-2}, and the model is integrated to a column density of 10^{23} cm^{-2}. The cloud velocity FWHM is 5 km s^{-1}. Whereas the results in § 4.2 were calculated for a fixed escape column, here the escape column is taken to be the column density into the cloud.

Figure 10 shows the temperature, electron fraction, and major atomic and molecular abundances as a function of depth into the cloud; it has been plotted on the same scale as Figure 3. If the model results depended solely on H_X/n (for a given density), the results shown in Figure 10 would exactly match those of Figure 3*a*. Variation in the net cooling rates due to the difference in column densities causes the depth-dependent results to differ somewhat from models in which H_X/n is varied by varying the X-ray flux at a fixed column. However, as comparison of Figure 3*a* and Figure 10 demonstrates, this deviation from perfect scaling with H_X/n or ξ_{eff} is quite minor, at least for this range of column densities. Hence, the primary parameter controlling the physical conditions in an XDR is the X-ray ionization parameter, expressed either as H_X/n or ξ_{eff}.

© American Astronomical Society • Provided by the NASA Astrophysics Data System

1996ApJ...466..561M

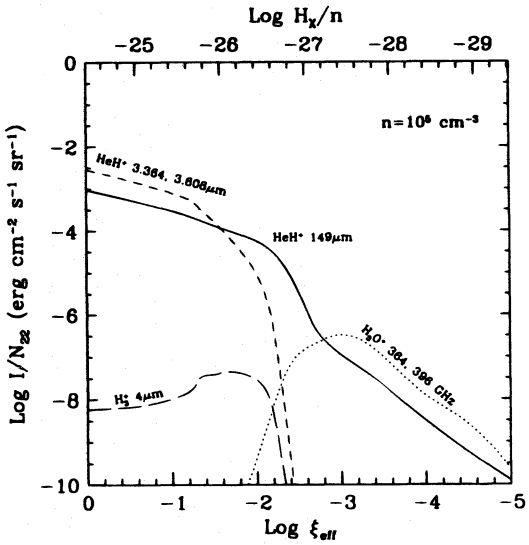

FIG. 9*a*

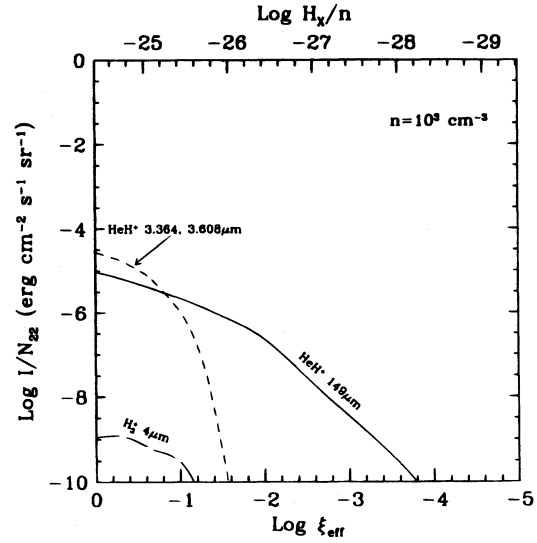

FIG. 9*b*

FIG. 9.—Estimated integrated intensities in the HeH^+ 149 μm rotation line and 3.364, 3.608 μm vibration lines, the H_3^+ vibration-rotation lines around 4 μm, and the 364 and 396 GHz transitions of H_3O^+ from a cloud of column 10^{22} cm^{-2}, as a function of ξ_{eff} and H_X/n. (*a*) $n = 10^5$ cm^{-3}. (*b*) $n = 10^3$ cm^{-3}.

4.4. *Comparison of XDR Spectra with Shock and PDR Spectra*

HM89 discuss various spectral discriminants between shocks and PDRs. These involve the H_2 $v = 2$–1 $S(1)/v = 1$–0 $S(1)$ ratio, the [O I] 63 μm/[C II] 158 μm ratio together with the [O I] 63 μm intensity, and the ([O I] 63 μm + [C II] 158 μm)/IR bolometric flux ratio. In addition, various authors (see, e.g., Moorwood & Oliva 1988; Kawara, Nishida, & Taniguchi 1988) have suggested that high [Fe II] 1.26 or 1.64 μm intensities are signatures of shocks. Here we summarize these diagnostics and discuss the identifying features of XDRs.

The H_2 2–1 $S(1)$/1–0 $S(1)$ ratio is of order 0.1 in 1000–2000 K gas where these lines are thermally excited and of order 0.5 when the H_2 vibrational lines result from fluorescence initiated by FUV photons. Therefore, this ratio has been used to discriminate between shocks (the former case) and PDRs (the latter case). HM89 showed that dissociative shocks could lead to ratios of order 0.5, but in this case the absolute intensities were relatively low ($\lesssim 10^{-4}$ ergs cm^{-2} s^{-1} sr^{-1}). Observationally, no shock with a ratio as high as 0.5 has been observed. On the other hand, Hollenbach (1988), Sternberg & Dalgarno (1989), and Burton, Hollenbach, & Tielens (1990) showed that dense PDRs could produce ratios ~0.1. Figure 11 shows the 2–1 $S(1)$/1–0 $S(1)$ ratio for densities $n = 10^5$ and $n = 10^3$ cm^{-3}; the tick marks on the curves show where the integrated intensity in

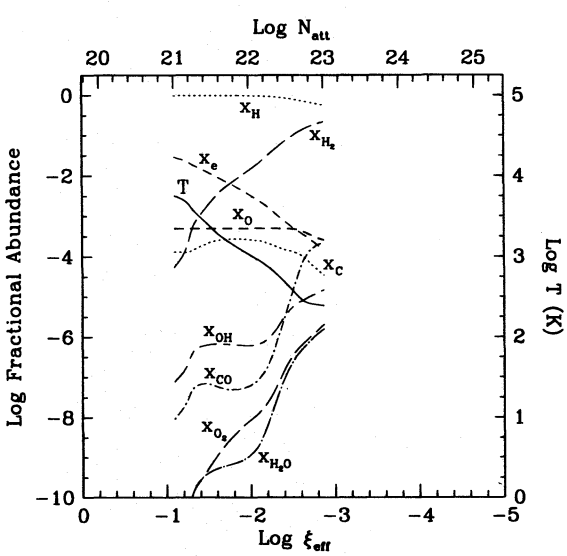

FIG. 10.—Depth-dependent XDR model. The initial attenuating column is 10^{21} cm^{-2}, and the model is integrated to a depth of 10^{23} cm^{-2}.

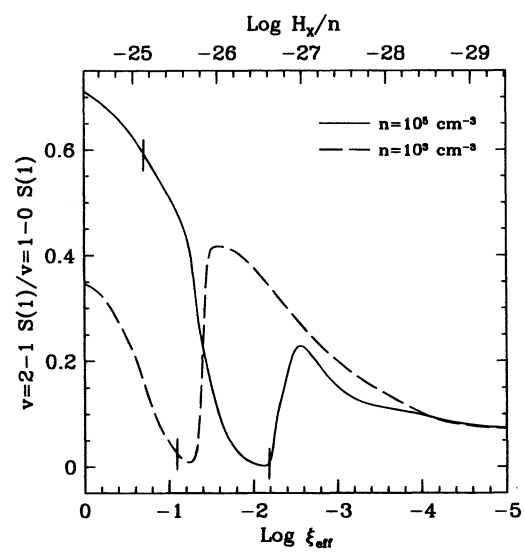

FIG. 11.—Ratio of the $v = 2$–1 $S(1)/v = 1$–0 $S(1)$ line as a function of ξ_{eff}. The solid line is for $n = 10^5$ cm^{-3}, and the dashed line is for $n = 10^3$ cm^{-3}. The emergent integrated intensity in the $v = 1$–0 $S(1)$ line $I \geq 10^{-3}$ ergs cm^{-2} s^{-1} sr^{-1} between the two tick marks on the curve for the $n = 10^5$ cm^{-3} model and to the left of the tick mark for the $n = 10^3$ cm^{-3} model.

© American Astronomical Society • Provided by the NASA Astrophysics Data System

1996ApJ...466..561M

the $v = 1$–0 $S(1)$ line exceeds 10^{-4} ergs cm^{-2} s^{-1} sr^{-1} (between the two tick marks for the $n = 10^5$ model; to the left of the tick mark for the $n = 10^3$ model: cf. Fig. 6). This figure shows that in XDRs, the H_2 2–1 $S(1)$/1–0 $S(1)$ ratio is nearly always $\lesssim 0.3$ and is generally ~ 0.1 where the intensity is high. Therefore, an observed ratio ~ 0.1 cannot discriminate among these regions, whereas a ratio of 0.5 would point to (low-density) PDRs. However, high values of the 2–1 $S(1)$/1–0 $S(1)$ ratio can be produced in high-density ($n \sim 10^5$ cm^{-3}) XDRs if the ionization parameter is high ($\xi_{\rm eff} \gtrsim 10^{-1.5}$); in this case, the high ratio is simply a reflection of the high gas temperature, as the H_2 vibrational levels are populated dominantly by thermal collisions.

When the [O I] 63 μm intensity is high ($I \gtrsim 10^{-3}$ ergs cm^{-2} s^{-1} sr^{-1}), the [O I] 63 μm/[C II] 158 μm ratio is higher in shocks ($\gtrsim 10$) than is generally found in PDRs ($\lesssim 10$). This is because shocks tend to be hotter than PDRs and because, for a given [O I] intensity, they are denser; the [O I] 63 μm/[C II] 158 μm ratio increases as n and T rise. In addition, in C shocks (Draine et al. 1983), the ratio is large because the C^+ abundance is much lower relative to the neutral O abundance. Figure 12 shows that, like shocks, XDRs generally show a large ratio ($\gtrsim 10$) when the [O I] 63 μm intensity exceeds 10^{-3} ergs cm^{-2} s^{-1} sr^{-1} (to the left of the tick marks on each curve: cf. Fig. 8), but there is some overlap with PDRs for low-density and high–column density XDRs with high values of $\xi_{\rm eff}$. In this latter case, we note that the XDR [O I] 145 μm/[O I] 63 μm ratio is moderately high ($\gtrsim 0.1$), compared with a ratio of 0.05–0.1 in PDRs (Fig. 13; tick marks as in Fig. 12). At the other extreme, we note that low-density XDRs with *low* $\xi_{\rm eff}$ can produce relatively high intensities ($\gtrsim 10^{-4}$ ergs cm^{-2} s^{-1} sr^{-1}) of [C II] 158 μm without appreciable [O I] 63 μm emission ([O I] 63 μm/[C II] 158 μm $< 10^{-2}$), as seen in Figure 8*b*. In shocks with these [C II] intensities, [O I] 63 μm/[C II] 158 μm $\gtrsim 10$, while in PDRs, [O I] 63 μm/[C II] 158 μm $\gtrsim 0.1$.

The flux ratio ([O I] 63 μm + [C II] 158 μm)/IR bolometric continuum is $\sim 10^{-3}$ to 10^{-2} in PDRs, while it is relatively unconstrained in shocks. Figure 14 shows that this ratio is often $10^{-0.5}$ to $10^{-1.5}$ in XDRs, but observationally one must be careful to eliminate any additional sources of IR continuum that might lie in the beam. Despite this caveat, ratios ~ 0.1 are strong signatures of XDRs.

Except for extremely high densities ($n \gtrsim 10^6$ cm^{-3}) and UV fields ($\gtrsim 10^5$ times the local ISRF), PDRs do not usually produce significant [Fe II] 1.26 or 1.64 μm emission (Burton et al. 1990). Shocks can produce strong [Fe II] emission (e.g., HM89), but again the energetic requirements are severe: to produce intensities $\gtrsim 10^{-3}$ ergs cm^{-2} s^{-1} sr^{-1}, the shocks must fill the beam and have preshock densities greater than 10^4 cm^{-3} and velocities $v_s \gtrsim 100$ km s^{-1}. However, Figure 6 shows that XDRs with $\xi_{\rm eff} \gtrsim 10^{-2}$, $N \gtrsim$

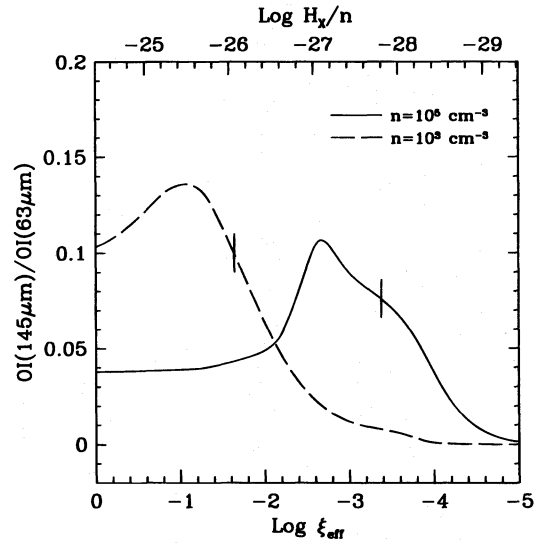

FIG. 13.—Ratio of the [O I] 145 μm/63 μm lines as a function of $\xi_{\rm eff}$. The solid line is for $n = 10^5$ cm^{-3}, and the dashed line is for $n = 10^3$ cm^{-3}. The emergent integrated intensity in the [O I] 63 μm line $I \geq 10^{-3}$ ergs cm^{-2} s^{-1} sr^{-1} to the left of the tick mark on each curve.

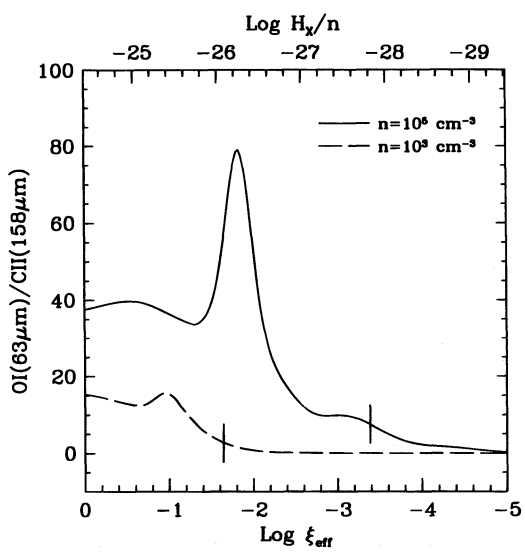

FIG. 12.—Ratio of the [O I] 63 μm/[C II] 158 μm lines as a function of $\xi_{\rm eff}$. The solid line is for $n = 10^5$ cm^{-3}, and the dashed line is for $n = 10^3$ cm^{-3}. The emergent integrated intensity in the [O I] 63 μm line $I \geq 10^{-3}$ ergs cm^{-2} s^{-1} sr^{-1} to the left of the tick mark on each curve.

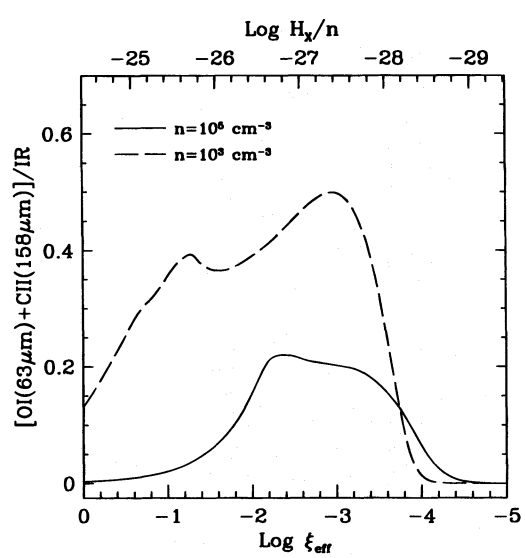

FIG. 14.—Ratio of the sum of the [O I] 63 μm and [C II] 158 μm lines to the infrared bolometric continuum as a function of $\xi_{\rm eff}$. Note that for both densities, this ratio exceeds ~ 0.1 over much of the modeled parameter space.

© American Astronomical Society • Provided by the NASA Astrophysics Data System

1996ApJ...466..561M

10^{22} cm^{-2}, and $n \gtrsim 10^4$ cm^{-3} will produce [Fe II] 1.26 and 1.64 μm intensities $\gtrsim 10^{-3}$ ergs cm^{-2} s^{-1} sr^{-1}. Strong [Fe II] emission may therefore be more often a signature of XDRs than shocks, and we speculate that the [Fe II] emission observed near AGNs is generally from XDRs, rather than shocks (see Blietz et al. 1994; Moorwood & Oliva 1994).

5. SUMMARY AND CONCLUSIONS

Hard X-ray photons ($E \gtrsim 1$ keV) are capable of traversing large column densities of gas before being absorbed photoelectrically and therefore can significantly heat and chemically affect large columns of gas. Since the sources of X-ray photons in astrophysics often have fairly flat spectral energy distributions (e.g., power-law continua in AGNs or bremsstrahlung emission from hot gas with a temperature of several keV), the X-ray energy deposition rates, and therefore the physical conditions, change only slowly with depth once the UV photons have been absorbed. These characteristics of X-ray dissociation regions (XDRs) are markedly different from the UV-dominated PDRs, in which the column density is limited to $N \sim$ a few $\times 10^{21}$ cm^{-2} by dust absorption, and the physical conditions change rapidly with depth because of the exponential dropoff of the incident UV photons due to dust absorption. In any region of column density $N \gtrsim 10^{22}$ cm^{-2} that is exposed to a fairly flat-spectrum source of UV and X-ray photons, the ionized zone will form only a thin skin on the surface of the XDR, a PDR will generally not be present, and the XDR will dominate the emission. Any interstellar cloud exposed to such a spectrum that has been filtered through a neutral column $N \gtrsim 10^{21}$ cm^{-2} will consist entirely of an XDR, with no ionized zone or PDR present at all. Thus, XDRs will dominate the emission whenever large columns of interstellar gas are exposed to a photon source with a moderately flat spectrum that extends to hard X-ray energies.

As we have shown in § 4, the main parameter controlling the physical state of X-ray–illuminated gas is the X-ray energy absorption rate per particle, H_X/n, or equivalently the effective ionization parameter $\xi_{\rm eff}$. Because the relative nonthermal electron loss processes depend so weakly on initial energy, it makes little difference how a given value of H_X/n was actually obtained (e.g., by attenuating a luminous hard X-ray source through a large column density or by filtering a weaker/softer source through a much smaller column). While the actual structure of an XDR will vary as the incident X-ray spectrum is varied, the local conditions at a fixed ionization parameter or energy deposition rate are largely independent of the spectrum.

We present models for a range 3.8×10^{-25} ergs cm^3 s$^{-1} \leq H_X/n \leq 3.8 \times 10^{-20}$ ergs cm^3 s^{-1}, or $10^{-5} \leq \xi_{\rm eff} \leq 1$. This range extends from substantially ionized ($x_e \sim 0.1$), 10^4 K gas to cold molecular gas with X-ray ionization rates $\zeta \sim 10^{-16}$ s^{-1} (approximately the local cosmic-ray ionization rate). Therefore, we have studied nearly the entire neutral (atomic or molecular) region of interest. At the highest values of H_X/n or $\xi_{\rm eff}$ we have modeled, the gas is atomic, warm ($T \approx 10^4$ K) and moderately ionized ($x_e \sim$ 0.01–0.1). As the local ionization parameter drops, the temperature and ionization fraction decline, and the molecular abundances increase. At the lowest values of H_X/n and $\xi_{\rm eff}$ that we consider, the gas is cold ($\sim$tens of kelvins), nearly all of the hydrogen is in H_2, most of the gas-phase carbon is in CO, and the ionization fraction is small ($x_e \sim$ few $\times 10^{-6}$). The atomic oxygen abundance always remains fairly substantial; the most important oxygen-containing molecules are CO, OH, H_2O, and O_2. Over most of the range in $\xi_{\rm eff}$ and H_X/n that we have modeled, most of the metal species which do not readily form molecules (Fe, S, and Si) are kept singly ionized by the locally generated UV photons.

In the warm atomic zone the primary coolants are Lyα, the [O I] 6300 Å line, and the far-red [C I] metastable lines. Because the gas temperature is close to 10^4 K, this region also produces intense emission from the J- and H-band lines of [Fe II] at 1.26 and 1.64 μm. As the ionization parameter decreases, there is a relatively narrow region of H_X/n or $\xi_{\rm eff}$ in which bright emission in the 2 μm vibration-rotation lines of H_2 is produced by thermal excitation. The H_2 abundance in this region is small, $x_{H_2} \sim 10^{-3}$ to 10^{-2}, and the H_2 2–1 $S(1)$/1–0 $S(1)$ ratio is generally $\sim$0.1. There is a secondary maximum in the H_2 line emission at lower $\xi_{\rm eff}$, where the excitation mechanism is collisional excitation of the vibrational levels by the *nonthermal* electrons; the peak intensity of this emission is typically 2–3 orders of magnitude lower than the thermally produced peak. At low ionization parameters, the emission is dominated by the pure rotational transitions of abundant molecules such as CO and by a number of mid- and far-infrared atomic fine-structure lines. A number of these fine-structure lines, especially the [O I] 63 μm line, the [Si II] 35 μm line, and the [C II] 158 μm line (depending on density) are very bright over a major fraction of our studied parameter space and are major coolants of the gas. Particularly noticeable in our XDR models are the very large emergent integrated intensities, with individual lines reaching 10^{-3} to 10^{-2} ergs cm^{-2} s^{-1} sr^{-1}, and the large line-to-continuum ratios for bright lines, up to $\sim$0.1.

XDRs are luminous sources of infrared and submillimeter emission lines. The high emergent surface brightnesses imply that a large number of these lines may be detectable from dense gas in the vicinity of bright X-ray sources, providing a large number of diagnostics of the physical conditions and the X-ray source parameters. We have previously used these models to study some aspects of the physics and chemistry of dense molecular "tori" around AGNs (Maloney et al. 1994; Maloney 1996) and water maser emission from high-pressure molecular tori and accretion disks in active galactic nuclei (Neufeld et al. 1994; Neufeld & Maloney 1995). We will make specific application of these models to other environments (e.g., giant molecular clouds in the disks of galaxies with active nuclei such as NGC 1068 and molecular gas near the Great Annihilator source in the Galactic center) in subsequent papers.

We would like to thank Steve Lepp, Alexander Dalgarno, Mark Voit, and David Neufeld for helpful discussions. D. J. H. benefited from discussions with Eduardo Iglesias in the very early stages of this project. We are grateful to Ralph Sutherland for his assistance in producing Figures 1 and 2. P. R. M. was supported by the NASA Astrophysical Theory Program through grant NAGW-766 and by the Long-Term Space Astrophysics Program through grant NAGW-4454. D. J. H. would like to acknowledge support through NASA RTOP 399-20-10-12 and RTOP 188-44-53-06.

© American Astronomical Society • Provided by the NASA Astrophysics Data System

1996ApJ...466..561M

APPENDIX A

IONIZATION AND HEATING RATES FOR POWER-LAW X-RAY SPECTRA

In calculating the depth dependence of the X-ray ionization and heating rates, it is necessary to assume a spectral shape. In this case we take the X-ray flux incident on the gas to be a power-law, with

$$F_i(E) = F_0\left(\frac{E}{1\ \mathrm{keV}}\right)^{-\alpha} . \tag{A1}$$

With increasing column density, the lowest energy photons are attenuated more and more heavily; the column density dependence of the X-ray heating and ionization rates is therefore a function of the slope of the X-ray energy spectrum.

To calculate the ionization and heating rates, we assume a normally incident flux of photons. The total (primary plus secondary) photoionization rate of hydrogen (neutral or molecular) is then given by

$$\zeta_T = \int_{E_{\min}}^{E_{\max}} \frac{F(E)}{E}\,[\sigma_{\mathrm{H}}(E) + \sigma_{\mathrm{pa}}(E)(E - E_{\mathrm{th}})N_{\mathrm{sec}}(E, x_e)]dE , \tag{A2}$$

where $F(E)$ is the *local* (i.e., attenuated) X-ray energy flux per unit energy, $\sigma_{\mathrm{H}}(E)$ is the photoionization cross section of hydrogen, σ_{pa} is the cross section due to all elements per hydrogen nucleus, E_{th} is the ionization threshold energy of the transition dominating the cross section at energy E, $N_{\mathrm{sec}}(E, x_e)$ is the number of secondary ionizations of hydrogen per unit energy produced by such a primary photoelectron of energy E, and $E_{\min}$ and $E_{\max}$ are the minimum and maximum X-ray photon energies. The former is set by the magnitude of the attenuating column; the latter is generally taken to be 100 keV, but for a power-law index $\alpha \sim 1$, as is typical for AGNs (so that there is roughly equal energy per decade of X-ray photon energy), the photoabsorption rates are very insensitive to $E_{\max}$ as long as $E_{\max} \gtrsim 30$ keV. $F(E)$ is related to the incident photon flux by

$$F(E) = F_i(E)e^{-\tau(E)} , \tag{A3}$$

where $\tau(E)$ is the optical depth corresponding to the column density between the source and the point in question. As in the text, we assume that the primary ionization rate of hydrogen is negligible compared to the secondary ionization rate and that Auger electrons contribute an energy equal to the photoionization threshold energy, so the total ionization rate simplifies to

$$\zeta_T \simeq N_{\mathrm{sec}}(x_e)\int_{E_{\min}}^{E_{\max}} \sigma_{\mathrm{pa}}(E)F(E)dE , \tag{A4}$$

where the integral is just the photoelectron energy deposition rate per particle H_{X} (eq. [1]), and N_{sec} has been taken to be independent of energy. This is a very good approximation for primary photoelectron energies between 0.1 and 10 keV (V91).

For the specific case of a power-law–incident X-ray spectrum, we have explicitly evaluated the integral in equation (A4) to obtain the column density dependence of the ionization and heating rates. Our adopted broken power-law fit to the cross section per H nucleus is

$$\sigma_{\mathrm{pa}}(E) = \sigma_0 E^{-\gamma} \tag{A5a}$$

$$\sigma_0 = 6.0 \times 10^{-23}\ \mathrm{cm}^2; \qquad \gamma = 3,\ 0.014 < E < 0.5\ \mathrm{keV} \tag{A5b}$$

$$\sigma_0 = 2.6 \times 10^{-22}\ \mathrm{cm}^2; \qquad \gamma = 8/3,\ 0.5 \le E \le 7\ \mathrm{keV} \tag{A5c}$$

$$\sigma_0 = 4.4 \times 10^{-22}\ \mathrm{cm}^2; \qquad \gamma = 8/3,\ 7\ \mathrm{keV} < E . \tag{A5d}$$

Equation (A5c) is accurate to 25% between 0.5 and 1 keV and to 10% between 1 and 7 keV. Equation (A5d) is accurate to 2% up to 10 keV. For energies below a few hundred eV, helium dominates the cross section; with increasing energy, the K-shell

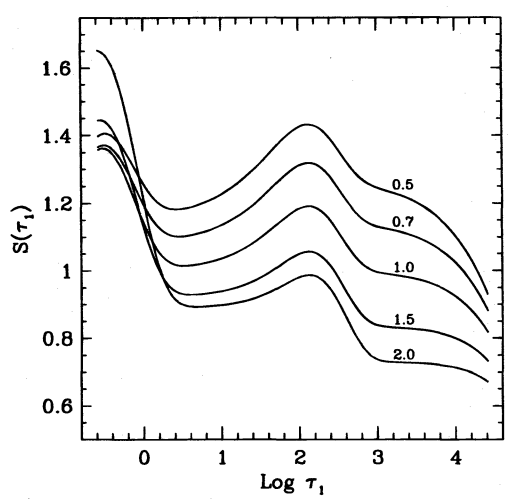

FIG. 15.—Dimensionless function S (see eq. [A7]) as a function of the 1 keV optical depth τ_1. The individual curves are labeled with the power-law index for the incident X-ray spectrum.

© American Astronomical Society • Provided by the NASA Astrophysics Data System

1996ApJ...466..561M

TABLE 3

ION-MOLECULE REACTIONS

Reaction	a^a(cm^3 s^{-1})
$H^+ + H \rightarrow H_2^+ + h\nu$	See text
$H^+ + CH \rightarrow CH^+ + H$	1.9(−9)
$H^+ + OH \rightarrow OH^+ + H$	2.1(−9)
$H^+ + H_2O \rightarrow H_2O^+ + H$	8.2(−9)
$H^+ + CH_2 \rightarrow CH^+ + H_2$	1.4(−9)
$He^+ + O_2 \rightarrow O^+ + O + He$	1.0(−9)
$He^+ + CO \rightarrow C^+ + O + He$	1.6(−9)
$He^+ + CH \rightarrow C^+ + H + He$	1.1(−9)
$He^+ + CH_2 \rightarrow CH^+ + H + He$	7.5(−10)
$He^+ + CH_2 \rightarrow C^+ + H_2 + He$	7.5(−10)
$He^+ + H_2O \rightarrow OH^+ + H + He$	3.7(−10)
$He^+ + H_2O \rightarrow H_2O^+ + He$	7.0(−11)
$He^+ + OH \rightarrow O^+ + H + He$	1.1(−9)
$C^+ + O_2 \rightarrow O^+ + CO$	4.1(−10)
$C^+ + O_2 \rightarrow CO^+ + O$	7.5(−10)
$C^+ + OH \rightarrow CO^+ + H$	7.7(−10)
$C^+ + H_2O \rightarrow HCO^+ + H$	2.7(−9)
$C^+ + CH \rightarrow CH^+ + C$	1.0(−9)
$C^+ + CH_2 \rightarrow CH_2^+ + C$	5.2(−10)
$O^+ + H_2 \rightarrow OH^+ + H$	1.6(−9)
$OH^+ + H_2 \rightarrow H_2O^+ + H$	1.1(−9)
$CO^+ + H \rightarrow CO + H^+$	7.5(−10)
$CO^+ + H_2 \rightarrow HCO^+ + H$	2.0(−9)
$HCO^+ + C \rightarrow CH^+ + CO$	1.1(−9)
$HCO^+ + CH \rightarrow CH_2^+ + CO$	6.3(−10)
$HCO^+ + OH \rightarrow H_2O^+ + CO$	6.2(−10)
$HCO^+ + CH_2 \rightarrow CH_3^+ + CO$	8.6(−10)
$HCO^+ + H_2O \rightarrow H_3O^+ + CO$	3.2(−9)
$H_2O^+ + H_2 \rightarrow H_3O^+ + H$	6.1(−10)
$H_2O^+ + C \rightarrow CH^+ + OH$	1.1(−9)
$H_2O^+ + CH \rightarrow CH_2^+ + OH$	3.4(−10)
$H_2O^+ + CH_2 \rightarrow CH_3^+ + OH$	4.7(−10)
$H_2O^+ + OH \rightarrow H_3O^+ + O$	6.9(−10)
$H_2O^+ + H_2O \rightarrow H_3O^+ + OH$	2.1(−9)
$H_2O^+ + CO \rightarrow HCO^+ + OH$	5.0(−10)
$H_3O^+ + C \rightarrow HCO^+ + H_2$	1.0(−11)
$H_3O^+ + CH \rightarrow CH_2^+ + H_2O$	6.8(−10)
$H_3O^+ + CH_2 \rightarrow CH_3^+ + H_2O$	9.4(−10)
$H_2^+ + H_2 \rightarrow H_3^+ + H$	2.1(−9)
$H_3^+ + C \rightarrow CH^+ + H_2$	2.0(−9)
$H_3^+ + O \rightarrow OH^+ + H_2$	8.0(−10)
$H_3^+ + CH \rightarrow CH_2^+ + H_2$	1.2(−9)
$H_3^+ + OH \rightarrow H_2O^+ + H_2$	1.3(−9)
$H_3^+ + CO \rightarrow HCO^+ + H_2$	1.7(−9)
$H_3^+ + H_2O \rightarrow H_3O^+ + H_2$	5.9(−9)
$H_3^+ + CH_2 \rightarrow CH_3^+ + H_2$	1.7(−9)
$CH_3^+ + O \rightarrow HCO^+ + H_2$	4.4(−10)
$CH^+ + H_2 \rightarrow CH_2^+ + H$	1.0(−9)
$CH^+ + O \rightarrow CO^+ + H$	7.6(−10)
$CH_2^+ + H_2 \rightarrow CH_3^+ + H$	7.2(−10)
$CH^+ + H \rightarrow C^+ + H_2$	2.0(−10)
$CO + OH^+ \rightarrow HCO^+ + O$	1.1(−9)
$CH_2^+ + O \rightarrow HCO^+ + H$	7.5(−10)

[a] Numbers in parentheses: $1.9(-9) = 1.9 \times 10^{-9}$. Rate coefficients have the form $k = aT_3^b e^{-c/T_3}$, where the gas temperature $T = 1000T_3$ K and a is in units of cm^3 s^{-1}.

opacities of metals such as carbon and oxygen dominate. The jump at 7 keV is due to iron.

It is convenient to change the integration variable from E to $u \equiv \tau_1 E_k^{-\gamma}$, $E_k = E/1$ keV, and $\tau_1 = 2.6N_{22}$ is the optical depth at 1 keV from the X-ray source to the point in question; N_{22} is the total attenuating hydrogen column $N_{\rm att}/10^{22}$ cm^{-2}. The total energy deposition rate per particle may then be written as

$$H_{\rm X} \simeq \frac{3\sigma_0 F_0}{8\tau_1^{\phi+1}} S(\tau_1) , \tag{A6}$$

where $\phi = (\alpha - 1)/\gamma$, and $S(\tau_1)$ is a dimensionless function of the integral of the X-ray spectrum over the cross section:

$$S(\tau_1) = \int_{u_{\rm min}}^{u_{\rm max}} u^{\phi} e^{-u} du , \tag{A7}$$

© American Astronomical Society • Provided by the NASA Astrophysics Data System

1996ApJ...466..561M

TABLE 4

ELECTRON RECOMBINATION REACTIONS

Reaction	a[a]	b
$H^+ + e^- \rightarrow H + h\nu$	1.3(−12)	−0.70
$O^+ + e^- \rightarrow O + h\nu$	1.7(−12)	−0.63
$C^+ + e^- \rightarrow C + h\nu$	2.1(−12)	−0.61
$OH^+ + e^- \rightarrow O + H$	1.1(−7)	−0.50
$CO^+ + e^- \rightarrow C + O$	9.9(−8)	−0.50
$H_2^+ + e^- \rightarrow H + H$	2.8(−8)	−0.37[b]
$H_3^+ + e^- \rightarrow H_2 + H$	6.0(−8)	−0.50[c]
$H_3^+ + e^- \rightarrow H + H + H$	6.0(−8)	−0.50[c]
$H_2O^+ + e^- \rightarrow OH + H$	1.1(−7)	−0.50
$H_2O^+ + e^- \rightarrow O + H_2$	1.1(−7)	−0.50
$HCO^+ + e^- \rightarrow CO + H$	8.1(−8)	−0.75
$H_3O^+ + e^- \rightarrow H_2O + H$	1.9(−7)	−0.50
$H_3O^+ + e^- \rightarrow OH + H + H$	3.6(−7)	−0.50
$CH^+ + e^- \rightarrow C + H$	5.5(−8)	−0.50
$CH_2^+ + e^- \rightarrow CH + H$	8.2(−8)	−0.50
$CH_2^+ + e^- \rightarrow C + H_2$	8.2(−8)	−0.50
$CH_3^+ + e^- \rightarrow CH_2 + H$	8.2(−8)	−0.50
$CH_3^+ + e^- \rightarrow CH + H + H$	8.2(−8)	−0.50
$Fe^+ + e^- \rightarrow Fe + h\nu$	1.7(−12)	−0.65
$Fe^{++} + e^- \rightarrow Fe^+ + h\nu$	7.8(−12)	−0.84
$Ni^+ + e^- \rightarrow Ni + h\nu$	1.8(−12)	−0.70
$Ni^{++} + e^- \rightarrow Ni^+ + h\nu$	5.0(−12)	−0.70
$Si^+ + e^- \rightarrow Si + h\nu$	2.4(−12)	−0.60
$Si^{++} + e^- \rightarrow Si^+ + h\nu$	6.1(−12)	−0.79
$S^+ + e^- \rightarrow S + h\nu$	1.7(−12)	−0.63
$S^{++} + e^- \rightarrow S^+ + h\nu$	8.7(−12)	−0.69

[a] Numbers in parentheses: $1.3(-12) = 1.3 \times 10^{-12}$. Rate coefficients have the form $k = aT_3^b e^{-c/T_3}$, where the gas temperature $T = 1000T_3$ K and a is in units of $cm^3\ s^{-1}$.

[b] Auerbach et al. 1977.

[c] Total rate coefficient is from Canosa et al. 1991; see text for discussion of branching ratios.

where $u_{min} = \tau_1 E_{k,max}^{-\gamma}$ and $u_{max} = \tau_1 E_{k,min}^{-\gamma}$. (Note that, because of the change of variables, F_0 must have dimensions of energy s^{-1} keV^{-1} for eq. [A6] to be dimensionally correct; H_X then has units of energy s^{-1}.) For $\phi > -1$, S can be expressed as the difference of incomplete gamma functions. S is always close to unity for $10^{-2} \lesssim \tau_1 \lesssim 10^4$ (Fig. 15). Note that the appropriate value of σ_0 is that of equation (A5c), and that our minimum value of $N_{att} \sim 10^{21}$ cm^{-2} corresponds to a minimum $\tau_1 \sim 0.3$. The optical depth scaling in equation (A6) indicates that H_X—and thus the ionization and heating rates—will scale with column density as $N^{-\phi-1} = N^{-(\alpha+\gamma-1)/\gamma}$. This is a relatively weak function of spectral index, varying from $N^{-0.8}$ for $\alpha = 0.5$ to $N^{-1.4}$ for $\alpha = 2$. We will usually take the spectral index to be $\alpha = 0.7$, the canonical X-ray index for AGNs (see e.g., Mushotzky 1982). Evaluating the constants, for $\alpha = 0.7$, the energy deposition rate per particle for a cloud that sees a normally incident 1–100 keV flux F_X ergs cm^{-2} s^{-1} is

$$H_X \simeq 4.2 \times 10^{-23} C_\alpha \frac{F_X}{N_{22}^{0.9}} S(\tau_1) \text{ ergs s}^{-1} , \tag{A8}$$

where C_α is a normalization constant for the X-ray spectrum, given by

$$C_\alpha = \frac{1-\alpha}{E_{k,max}^{1-\alpha} - E_{k,min}^{1-\alpha}} \qquad (\alpha \neq 1)$$

$$C_\alpha = (\ln E_{k,max}/E_{k,min})^{-1} \qquad (\alpha = 1) , \tag{A9}$$

TABLE 5

NEUTRAL-NEUTRAL REACTIONS

Reaction	a[a]	b
$C + OH \rightarrow CO + H$	2.0(−10)	0.50
$C + O_2 \rightarrow CO + O$	6.0(−11)	0.50
$O + CH \rightarrow CO + H$	1.7(−10)	0.50
$O + CH \rightarrow HCO^+ + e^-$	4.4(−11)	0.50
$O + CH_2 \rightarrow CO + H + H$	7.3(−11)	0.50
$H + H + H \rightarrow H_2$	5.5(−32)	1.00[b]

[a] Numbers in parentheses: $2.0(-10) = 2.0 \times 10^{-10}$. Rate coefficients have the form $k = aT_3^b e^{-c/T_3}$, where the gas temperature $T = 1000T_3$ K and a is in units of $cm^3\ s^{-1}$.

[b] Jacobs, Giedt, & Cohen 1967.

© American Astronomical Society • Provided by the NASA Astrophysics Data System

1996ApJ...466..561M

TABLE 6

CHARGE EXCHANGE REACTIONS

Reaction	a[a]	b	c
$H^+ + O \rightarrow O^+ + H$	7.0(−10)	...	0.230
$H^+ + S \rightarrow S^+ + H$	1.3(−9)	...	...
$H^+ + Si \rightarrow Si^+ + H$	9.9(−10)	...	...
$H^+ + Fe \rightarrow Fe^+ + H$	7.4(−9)	...	...
$He^+ + Si \rightarrow Si^+ + He$	3.3(−9)	...	...
$C^+ + S \rightarrow S^+ + C$	1.5(−9)	...	...
$C^+ + Si \rightarrow Si^+ + C$	2.1(−9)	...	...
$C^+ + Fe \rightarrow Fe^+ + C$	2.6(−9)	...	...
$S^+ + Si \rightarrow Si^+ + S$	1.6(−9)	...	...
$S^+ + Fe \rightarrow Fe^+ + S$	1.8(−10)	...	...
$Si^+ + Fe \rightarrow Fe^+ + Si$	1.9(−10)	...	...
$Fe^{++} + H \rightarrow Fe^+ + H^+$	1.9(−10)	0.17[b]	...
$Fe^+ + H^+ \rightarrow Fe^{++} + H$	2.0(−9)	...	30.054[b]
$S^{++} + H \rightarrow S^+ + H^+$	1.0(−14)[c]	...	...
$Ni^{++} + H \rightarrow Ni^+ + H^+$	5.3(−10)	0.62[b]	...
$Si^{++} + H \rightarrow Si^+ + H^+$	2.5(−9)	0.28[d]	...
$Si^+ + H^+ \rightarrow Si^{++} + H$	8.3(−10)	0.28	31.75[d]
$H_2^+ + H \rightarrow H^+ + H_2$	6.4(−10)	...	...
$H_2O^+ + Si \rightarrow Si^+ + H_2O$	3.0(−9)	...	...
$H_2O^+ + S \rightarrow S^+ + H_2O$	4.3(−10)	...	...
$H_2O^+ + Fe \rightarrow Fe^+ + H_2O$	1.5(−9)	...	...
$H_2O^+ + CH \rightarrow CH^+ + H_2O$	3.4(−10)	...	...
$H_2O^+ + CH_2 \rightarrow CH_2^+ + H_2O$	4.7(−10)	...	...
$HCO^+ + Fe \rightarrow Fe^+ + HCO$	1.9(−9)	...	...

[a] Numbers in parentheses: $1.0(-10) = 1.0 \times 10^{-10}$. Rate coefficients have the form $k = aT_3^b e^{-c/T_3}$, where the gas temperature $T = 1000T_3$ K and a is in units of $cm^3\ s^{-1}$.
[b] Neufeld & Dalgarno 1987.
[c] A. Dalgarno, private communication.
[d] Gargaud, McCarroll, & Valiron 1982.

while the hydrogen ionization rate (per nucleon) is

$$\zeta_T \simeq 1.83 \times 10^{10}\left(\frac{f_i}{0.4}\right)H_X$$

$$\simeq 7.7 \times 10^{-13}C_\alpha\left(\frac{f_i}{0.4}\right)\frac{F_X}{N_{22}^{0.9}}\ s^{-1}\ , \tag{A10}$$

where f_i is the fraction of primary photoelectron energy that goes into ionization. For $\alpha = 0.7$, $E_{min} = 1$ keV, $E_{max} = 100$ keV, $C_\alpha = 0.101$. The heating rate is identical in form to the ionization rate except that N_{sec} is replaced by f_h, the fraction of primary

TABLE 7

REACTIONS WITH AN ACTIVATION BARRIER

Reaction	a[a]	b	c
$H_2 + O \rightarrow OH + H$	2.3(−11)	1.53	4.06[b]
$H + OH \rightarrow H_2 + O$	4.2(−12)	1.53	2.97[b]
$H_2 + OH \rightarrow H_2O + H$	9.2(−12)	1.95	1.42[b]
$H_2O + H \rightarrow H_2 + OH$	4.9(−11)	1.57	9.13[b]
$H + O_2 \rightarrow OH + O$	5.5(−10)	−0.90	8.75[b]
$O + OH \rightarrow H + O_2$	2.4(−11)	−0.50	0.03[b]
$OH + OH \rightarrow H_2O + O$	9.7(−13)	2.04	−0.87[b,c]
$O + H_2O \rightarrow OH + OH$	1.1(−11)	1.75	7.86[b]
$H_2 + O_2 \rightarrow OH + OH$	4.2(−12)	...	9.30
$H_2 + C \rightarrow CH + H$	4.0(−9)	1.0	14.0
$H + CH \rightarrow H_2 + C$	3.1(−11)	0.50	2.20
$H_2 + CH \rightarrow CH_2 + H$	4.9(−11)	0.67	8.80
$H + CH_2 \rightarrow H_2 + CH$	4.9(−11)	0.67	13.0
$C^+ + H_2 \rightarrow CH^+ + H$	2.0(−10)	...	4.64[d]
$H^+ + CO \rightarrow H + CO^+$	1.9(−10)	...	4.66
$H + OH^+ \rightarrow H_2 + O^+$	3.7(−10)	...	7.40
$H + CO \rightarrow C + OH$	2.0(−10)	0.50	77.7
$CH_2^+ + H \rightarrow CH^+ + H_2$	4.3(−10)	−0.25	1.32

[a] Numbers in parentheses: $2.3(-11) = 2.3 \times 10^{-11}$. Rate coefficients have the form $k = aT_3^b e^{-c/T_3}$, where the gas temperature $T = 1000T_3$ K and a is in units of $cm^3\ s^{-1}$.
[b] Vibrationally cold rate coefficients from Wagner & Graff 1987.
[c] For $T_3 \geq 0.3$; for $T_3 < 0.3$ the rate coefficient is fixed at the $T_3 = 0.3$ value.
[d] Hollenbach & McKee 1989, following Draine & Katz 1986.

© American Astronomical Society • Provided by the NASA Astrophysics Data System

1996ApJ...466..561M

TABLE 8

REACTIONS OF VIBRATIONALLY EXCITED HYDROGEN

Reaction	a[a]	b	c
$H_2^* + O \rightarrow OH + H$	2.4(−11)	1.93	3.94[b]
$H_2^* + OH \rightarrow H_2O + H$	7.7(−12)	2.35	1.21[b]
$H_2^* + C \rightarrow CH + H$	2.2(−9)	0.50	8.0
$H_2^* + CH \rightarrow CH_2 + H$	4.9(−11)	0.67	0.0
$H_2^* + C^+ \rightarrow CH^+ + H$	2.0(−10)[c]	...	...

[a] Numbers in parentheses: 2.4(−11) = 2.4×10^{-11}. Rate coefficients have the form $k = aT_3^b e^{-c/T_3}$, where the gas temperature $T = 1000T_3$ K and a is in units of $cm^3\ s^{-1}$.

[b] Rate coefficients from Wagner & Graff 1987.

[c] Hollenbach & McKee 1989, following Draine & Katz 1986.

photoelectron energy that goes into gas heating. The X-ray heating rate per unit volume may be written

$$n\Gamma_X \simeq 3 \times 10^4 \left(\frac{f_h}{0.3}\right) n_5 H_X$$

$$\simeq 1.2 \times 10^{-18} C_\alpha n_5 \left(\frac{f_h}{0.3}\right) \frac{F_X}{N_{22}^{0.9}} \text{ ergs cm}^{-3}\text{ s}^{-1}\ , \tag{A11}$$

where the total density of hydrogen nuclei $n = 10^5 n_5$ cm^{-3}. In equations (A10) and (A11) we have normalized f_i and f_h to typical values for low ionization fractions (SvS85; XM91; V91).

Above $E \sim 10$ keV, Compton scattering dominates over photoelectric absorption. At these energies, the energy deposition as a function of column density is qualitatively different, as the energy loss per scattering is small. Also, since energetic X-rays interact with bound and free electrons impartially, most of the scattering occurs off of electrons bound to hydrogen, rather than to metals. To get an approximate estimate of the rates of Compton ionization and heating, we assume that the spectral energy distribution is unaltered by the Compton scattering, i.e., the Compton optical depth is small. We have evaluated these rates including Klein-Nishina corrections up to third order in $E/m_e c^2$, so the error in the cross section is less than 5% for $E < 100$ keV. The Compton heating and ionization rates can be expressed in a form similar to equation (A8), with $S(\tau_1)$ replaced by a more complicated dimensionless integral over the X-ray spectrum. Since for our assumed spectral slope the total X-ray photon energy is (weakly) dominated by the most energetic photons, the Compton results are somewhat sensitive to the maximum X-ray photon energy E_{max}. However, the effect of Compton scattering is minor for columns $N \lesssim 10^{24}$ that we consider in this paper.

APPENDIX B

CHEMISTRY

Our chemical network currently incorporates 38 species and 157 chemical and photoreactions. The X-ray ionization and UV ionization and dissociation reaction rates are discussed in § 2.1. Our adopted chemical rates are listed in Tables 3–9. All

TABLE 9

REACTIONS OF NEGATIVE IONS

Reaction	a[a]	b	c
$H + e^- \rightarrow H^- + h\nu$	See text		
$H + H^- \rightarrow H_2 + e^-$	1.5(−9)	...	...
$H^+ + H^- \rightarrow H + H$	1.3(−7)	−0.50	...
$H_2^+ + H^- \rightarrow H_2 + H$	1.3(−7)	−0.50	...
$H_3^+ + H^- \rightarrow H_2 + H_2$	1.3(−7)	−0.50	...
$He^+ + H^- \rightarrow He + H$	1.3(−7)	−0.50	...
$O + H^- \rightarrow OH + e^-$	1.0(−9)	...	...
$C + H^- \rightarrow CH + e^-$	1.0(−9)	...	...
$C^+ + H^- \rightarrow C + H$	1.3(−7)	−0.50	...
$O^+ + H^- \rightarrow O + H$	1.3(−7)	−0.50	...
$S^+ + H^- \rightarrow S + H$	1.3(−7)	−0.50	...
$Si^+ + H^- \rightarrow Si + H$	1.3(−7)	−0.50	...
$Fe^+ + H^- \rightarrow Fe + H$	1.3(−7)	−0.50	...
$OH + H^- \rightarrow H_2O + e^-$	1.0(−10)	...	...
$HCO^+ + H^- \rightarrow CO + H_2$	1.3(−7)	−0.50	...
$H_3O^+ + H^- \rightarrow OH + H_2 + H$	1.3(−7)	−0.50	...
$H_3O^+ + H^- \rightarrow H_2O + H_2$	1.3(−7)	−0.50	...

NOTE.—Numbers in parentheses: 1.5(−9) = 1.5×10^{-9}. Rate coefficients have the form $k = aT_3^b e^{-c/T_3}$, where the gas temperature $T = 1000T_3$ K and a is in units of $cm^3\ s^{-1}$.

© American Astronomical Society • Provided by the NASA Astrophysics Data System

1996ApJ...466..561M

TABLE 10

REACTIONS WITH GRAINS

Reaction	$k_{gr,i}$ (cm^3 s^{-1})
$H^+ + \text{grain} \rightarrow \text{grain}^+ + H$	$k_{gr,1} = 7.6 \times 10^{-8}(a_{min}/10\ \text{Å})^{3/2}$
$M^+ + \text{grain} \rightarrow \text{grain}^+ + M$	$k_{gr,2} = (m_H/m_M)^{1/2}k_{gr,1}$
$e^- + \text{grain}^+ \rightarrow \text{grain}$	$k_{gr,3} = 2.1 \times 10^{-5}(a_{min}/10\ \text{Å})T_3^{-1/2}$
$H^+ + \text{grain}^- \rightarrow \text{grain} + H$	$k_{gr,4} = 4.9 \times 10^{-7}(a_{min}/10\ \text{Å})T_3^{-1/2}$
$M^+ + \text{grain}^- \rightarrow \text{grain} + M$	$k_{gr,5} = (m_H/m_M)^{1/2}k_{gr,4}$
$e^- + \text{grain} \rightarrow \text{grain}^-$	$k_{gr,6} = 3.2 \times 10^{-6}(a_{min}/10\ \text{Å})^{3/2}$
$h\nu(\text{FUV}) + \text{grain} \rightarrow \text{grain}^+$	$k_{gr,7} = 1.0 \times 10^{-7}(G_0/n)(f_y/10)(a_{min}/10\ \text{Å})^3$
$h\nu(\text{FUV}) + \text{grain}^- \rightarrow \text{grain}$	$k_{gr,8} = k_{gr,8}$

NOTE.—a_{min} is the minimum grain radius. M denotes an ion of mass m_M, while m_H is the mass of a hydrogen atom. f_y is a yield enhancement factor for small grains over bulk materials (see text).

rate coefficients are given in the form $k = aT_3^b e^{-c/T_3}$, where the gas temperature $T = 1000T_3$ K and a is in units of cm^3 s^{-1}. Unless noted otherwise, these rate coefficients are from the compilation of Millar et al. (1991). Aside from recombination on grains (see Appendix C), we have ignored grain-surface chemistry, with the exception of grain surface formation of H_2. The temperature dependence of the H_2 grain formation rate coefficient is very uncertain, and we have neglected any such dependence and adopted a constant value of 3×10^{-17} cm^3 s^{-1} for the rate coefficient. Many of our results are insensitive to this choice; for example, at elevated temperatures ($T \gtrsim 2000$ K), H_2 formation is dominated by reaction of H^- with H rather than grain surface formation.

The temperature dependence of the radiative association reaction

$$H^+ + H \rightarrow H_2^+ + h\nu \tag{B1}$$

is complicated; we have adopted the expression of Latter (1989), which matches the calculations of Bates (1951). For the formation of the H^- ion by radiative association,

$$H + e^- \rightarrow H^- + h\nu\ , \tag{B2}$$

we have numerically fitted the calculations of de Jong (1972).

As noted earlier, we have adopted the moderately fast rate of Canosa et al. (1991) for dissociative recombination of H_3^+. There are two possible reaction channels:

$$H_3^+ + e \rightarrow H_2 + H \tag{B3}$$

$$H_3^+ + e \rightarrow H + H + H\ . \tag{B4}$$

The actual branching fraction has recently been determined by Datz et al. (1995); below about 3500 K, channel (B3) occurs 25% of the time. We have used a numerical fit to the results of Datz et al. to evaluate the branching ratios.

Our adopted rate coefficients generally assume that molecules are vibrationally cold; however, we have specifically included reactions with vibrationally excited molecular hydrogen, H_2^* (Table 8). The fraction of H_2 in excited vibrational states is explicitly calculated at each point, with the simplifying assumption that the chemistry does not affect this fraction. For oxygen-containing species, we have used the rate coefficients of Wagner & Graff (1987). For carbon-containing species (specifically, reactions of H_2^* with C, C^+, and CH), we have reduced the activation energies for the relevant reactions by $E/k = 6000$ K, the approximate energy of the $v = 1$ level above ground. In contrast to PDRs, where vibrationally excited molecular hydrogen is produced by UV pumping and the average vibrational quantum number $\langle v \rangle \sim 6$ (Tielens & Hollenbach 1985), excitation of the vibrational states in XDRs is due to collisions, and most of the excited molecules are in $v = 1$.

APPENDIX C

GRAIN SURFACE REACTIONS

As mentioned in § 2.4.2, recombination of ions on grain surfaces can become a major ionic loss route once the electron fraction drops below $x_e \sim 10^{-3}$. For a standard grain size distribution, with $n(a) \propto a^{-3.5}$, recombination on grains is dominated by the smallest grains, as they provide most of the grain surface area. We calculate the rate at which ions recombine on grains and the grain charge distribution (neutral or singly positively or negatively charged) following Draine & Sutin (1987) and Bakes & Tielens (1994). Table 10 lists the adopted rates for reactions involving grains. We have adopted a minimum grain radius $a_{min} = 10$ Å (§ 2.4.2). In Table 10, M denotes an ion (atomic or molecular) with mass m_M. The factor f_y in the seventh equation of Table 10 is a yield enhancement factor for small grains over bulk materials; for a grain radius $a = 10$ Å, $f_y = 8.8$ (cf. Bakes & Tielens, eq. [16]). For our adopted size distribution, the total abundance of grains is

$$x_{gr} = 1.9 \times 10^{-8}\left(\frac{10\ \text{Å}}{a_{min}}\right)^{2.5} \tag{C1}$$

relative to the density of hydrogen nuclei n.

© American Astronomical Society • Provided by the NASA Astrophysics Data System

1996ApJ...466..561M

REFERENCES

Aitken, D. K., & Roche, P. F. 1985, MNRAS, 213, 777
Auerbach, D., Cacak, R., Caudano, R., Gaily, T. D., Keyser, C. J., McGowan, J. W., Mitchell, J. B. A., & Wilk, S. F. J. 1977, J. Phys. B, 10, 3797
Bakes, E. L. O., & Tielens, A. G. G. M. 1994, ApJ, 427, 822
Bates, D. R. 1951, J. Chem. Phys., 19, 1122
Black, J. H. 1987, in Interstellar Processes, ed. D. J. Hollenbach & H. A. Thronson (Dordrecht: Reidel), 731
Black, J. H., Porter, A., & Dalgarno, A. 1981, ApJ, 249, 138
Black, J. H., & van Dishoeck, E. F. 1987, ApJ, 322, 412
Blietz, M., Cameron, M., Drapatz, S., Genzel, R., Krabbe, A., van der Werf, P., Sternberg, A., & Ward, M. 1994, ApJ, 421, 92
Burton, M. G., Hollenbach, D. J., & Tielens, A. G. G. M. 1990, ApJ, 365, 620
Canosa, A., Rowe, B. R., Mitchell, J. B. A., Gomet, J. C., & Rebrion, C. 1991, A&A, 248, L19
Cecchi-Pestellini, C., & Dalgarno, A. 1993, ApJ, 413, 611
Cravens, T. E., & Dalgarno, A. 1978, ApJ, 279, 750
Cravens, T. E., Victor, G. A., & Dalgarno, A. 1975, Planet. Space Sci., 23, 1059
Datz, S., Sundstrom, G., Biedermann, Ch., Broström, L., Danared, H., Mannerick, S., Mowat, J. R., & Larsson, M. 1995, Phys. Rev. Lett., 74, 876
de Jong, T. 1972, A&A, 20, 263
Draine, B. T., & Katz, N. 1986, ApJ, 306, 655
Draine, B. T., Roberge, W. G., & Dalgarno, A. 1983, ApJ, 264, 485
Draine, B. T., & Sutin, B. 1987, ApJ, 320, 803
Draine, B. T., & Woods, D. T. 1989, in Infrared Spectroscopy in Astronomy, ed. B. H. Kaldeich (ESA SP 290) (Noordwijk: ESA), 155
———. 1990, ApJ, 363, 464
———. 1991, ApJ, 383, 621
Elitzur, M. 1991, Astronomical Masers (Dordrecht: Kluwer)
Gargaud, M., McCarroll, R., & Valiron, P. 1982, A&A, 106, 197
Glassgold, A. E., & Langer, W. D. 1973, ApJ, 186, 859
Gredel, R., & Dalgarno, A. 1995, ApJ, 446, 852
Gredel, R., Lepp, S., & Dalgarno, A. 1987, ApJ, 323, L137
Gredel, R., Lepp, S., Dalgarno, A., & Herbst, E. 1989, ApJ, 347, 289
Hollenbach, D. J. 1988, Astrophys. Lett. Commun., 26, 191
Hollenbach, D., & McKee, C. F. 1979, ApJS, 41, 555
———. 1989, ApJ, 342, 306 (HM89)
Jacobs, T. A., Giedt, R. R., & Cohen, N. 1967, J. Chem. Phys., 47, 54
Jenkins, E. B. 1989, in Interstellar Dust, ed. L. J. Allamandola & A. G. G. M. Tielens (Dordrecht: Kluwer), 23
Kawara, N., Nishida, M., & Taniguchi, Y. 1988, ApJ, 328, L41
Krolik, J. H., & Begelman, M. C. 1988, ApJ, 329, 702
Krolik, J. H., & Kallman, T. R. 1983, ApJ, 267, 610
Krolik, J. H., & Lepp, S. 1989, ApJ, 347, 179
Latter, W. B. 1989, Ph.D. thesis, Univ. of Arizona
Lennon, M. A., Bell, K. L., Gilbody, H. B., Hughes, J. G., Kingston, A. E., Murray, M. J., & Smith, F. J. 1988, J. Phys. Chem. Ref. Data, 17, 1285
Lepp, S., & McCray, R. 1983, ApJ, 269, 560
Lepp, S., & Shull, J. M. 1983, ApJ, 270, 578
Maloney, P. R. 1996, in Cygnus A—A Study of a Radio Galaxy, ed. C. Carilli & D. Harris (Cambridge: Cambridge Univ. Press), 60
Maloney, P. R., Begelman, M. C., & Rees, M. J. 1994, ApJ, 432, 606
Maloney, P. R., Hollenbach, D. J., & Tielens, A. G. G. M. 1996, in preparation
Millar, T. J., Rawlings, J. M. C., Bennett, A., Brown, P. D., & Charnley, S. B. 1991, A&AS, 87, 585
Moorwood, A. F. M., & Oliva, E. 1988, A&A, 203, 278
———. 1994, ApJ, 429, 602
Morrison, R., & McCammon, D. 1983, ApJ, 270, 119
Mushotzky, R. F. 1982, ApJ, 256, 92
Mushotzky, R. F., Done, C., & Pounds, K. A. 1993, ARA&A, 31, 717
Neufeld, D. A., & Dalgarno, A. 1987, Phys. Rev. A, 35, 3142
Neufeld, D. A., & Kaufman, M. J. 1993, ApJ, 418, 263
Neufeld, D. A., & Maloney, P. R. 1995, ApJ, 447, L17
Neufeld, D. A., Maloney, P. R., & Conger, S. 1994, ApJ, 436, L127
Phillips, T. G., van Dishoeck, E. F., & Keene, J. C. 1992, ApJ, 399, 533
Pollack, J. B., Hollenbach, D., Beckwith, S., Simonelli, D. P., Roush, T., & Fong, W. 1994, ApJ, 421, 615
Pradhan, A. K., & Zhang, H. L. 1993, ApJ, 409, L77
Prasad, S. S., & Tarafdar, S. P. 1983, ApJ, 267, 603
Roche, P. F. 1989, in Interstellar Dust, ed. L. J. Allamandola & A. G. G. M. Tielens (Dordrecht: Kluwer), 303
Shull, J. M., & van Steenberg, M. E. 1985, ApJ, 298, 268 (SvS85)
Stephens, T. L., & Dalgarno, A. 1973, ApJ, 186, 165
Sternberg, A., & Dalgarno, A. 1989, ApJ, 338, 197
Tarter, C. B., Tucker, W. H., & Salpeter, E. E. 1969, ApJ, 156, 943
Tielens, A. G. G. M., & Hollenbach, D. 1985, ApJ, 291, 722
van Steenberg, M. E., & Shull, J. M. 1988, ApJ, 330, 942
Verner, D. A., Yakovlev, D. G., Band, I. M., & Trzhaskovskaya, M. B. 1993, At. Data Nucl. Data Tables, 55, 233
Voit, G. M. 1991a, ApJ, 377, 158 (V91)
———. 1991b, ApJ, 379, 122
Wagner, A. F., & Graff, M. M. 1987, ApJ, 317, 423
Xu, Y., & McCray, R. 1991, ApJ, 375, 190 (XM91)
Zhang, H. L., & Pradhan, A. K. 1994, A&A, 293, 953

© American Astronomical Society • Provided by the NASA Astrophysics Data System